

Overcoming Resolution Attenuation During Tilted Cryo-EM Data Collection

Sriram Aiyer¹, Philip R. Baldwin^{1,2}, Shi Min Tan³, Zelin Shan¹, Juntaek Oh⁴, Atousa Mehrani¹, Marianne E Bowman⁵, Gordon Louie⁵, Dario Oliveira Passos¹, Selena Đorđević-Marquardt¹, Mario Mietzsch⁶, Joshua A. Hull⁶, Shuichi Hoshika⁷, Benjamin A. Barad⁸, Danielle A. Grotjahn⁸, Robert McKenna⁶, Mavis Agbandje-McKenna⁶, Steven A. Benner⁷, Joseph A. P. Noel^{5,9}, Dong Wang^{4,9,10}, Yong Zi Tan^{3,11,12,#}, Dmitry Lyumkis^{1,8,13#}

1. Laboratory of Genetics, The Salk Institute for Biological Studies, La Jolla, CA 92037, USA.
2. Department of Biochemistry and Molecular Biology, Baylor College of Medicine, Houston, TX 77030, USA.
3. Department of Biological Sciences, National University of Singapore, 16 Science Drive 4, Singapore 117558, Singapore.
4. Division of Pharmaceutical Sciences, Skaggs School of Pharmacy & Pharmaceutical Sciences, University of California, San Diego, La Jolla, CA, 92093, USA.
5. Jack H. Skirball Center for Chemical Biology and Proteomics, The Salk Institute for Biological Studies, La Jolla, CA 92037, USA.
6. Department of Biochemistry and Molecular Biology, College of Medicine, University of Florida, Gainesville, FL 32610.
7. Foundation for Applied Molecular Evolution, 13709 Progress Blvd Box 7, Alachua, FL 32615, USA.
8. Department of Integrative Structural and Computational Biology, The Scripps Research Institute, La Jolla, CA 92037, USA.
9. Department of Chemistry and Biochemistry, University of California San Diego, La Jolla, CA 92093, USA.
10. Department of Cellular and Molecular Medicine, University of California, San Diego, La Jolla, CA 92093, USA.
11. Disease Intervention Technology Laboratory (DITL), Agency for Science, Technology and Research (A*STAR), 8A Biomedical Grove, Singapore 138648, Singapore.
12. Institute of Molecular and Cell Biology (IMCB), Agency for Science, Technology and Research (A*STAR), 61 Biopolis Drive, Proteos, Singapore 138673, Republic of Singapore.
13. Graduate School of Biological Sciences, Section of Molecular Biology, University of California San Diego, La Jolla, CA 92093, USA.

#For materials and correspondence: Dmitry Lyumkis (dlyumkis@salk.edu), Yong Zi Tan (yztan@nus.edu.sg)

Keywords: Preferred orientation, orientation anisotropy, resolution anisotropy, Fourier Shell Correlation, stage tilts, single-particle cryo-EM analysis, resolution attenuation

1 **Abstract**

2

3 Structural biology efforts using cryogenic electron microscopy are frequently stifled by
4 specimens adopting “preferred orientations” on grids, leading to anisotropic map resolution and
5 impeding structure determination. Tilting the specimen stage during data collection is a generalizable
6 solution but has historically led to substantial resolution attenuation. Here, we develop updated data
7 collection and image processing workflows and demonstrate, using multiple specimens, that
8 resolution attenuation is negligible or significantly reduced across tilt angles. Reconstructions with
9 and without the stage tilted as high as 60° are virtually indistinguishable. These strategies allowed the
10 reconstruction to 3 Å resolution of a bacterial RNA polymerase with preferred orientation.
11 Furthermore, we present a quantitative framework that allows cryo-EM practitioners to define an
12 optimal tilt angle for dataset acquisition. These data reinforce the utility of employing stage tilt for
13 data collection and provide quantitative metrics to obtain isotropic maps.

14

15

1 **Introduction**

2

3 Single-particle cryogenic electron microscopy (cryo-EM) has become a mainstream tool for
4 macromolecular structural biology. Cryo-EM reconstructions resolved to near-atomic resolution are
5 now routine and have shed light on many important biological phenomena^{1,2}. Hardware and software
6 advances have collectively led to the advent of true atomic resolution, where individual atoms are
7 observed and distinguished within reconstructed maps³⁻⁶. Moreover, modern cryo-EM workflows
8 allow users to gain insight into macromolecular structural heterogeneity, for example to help identify
9 binding factors or to infer dynamics⁷. These and other capabilities demonstrate the power and the
10 potential of the technique to visualize macromolecular machines, to explain their function with
11 atomic-level precision, and to describe biological processes in dynamic terms.

12

13 Sample preparation for cryo-EM imaging requires first the vitrification of purified
14 macromolecules within a thin aqueous layer. Subsequently, 2D projection images of individual
15 macromolecular particles are recorded using a transmission electron microscope equipped with an
16 electron detector. Assuming a homogenous particle subset, the projections differ depending on the
17 orientation of each particle within the ice layer with respect to the electron beam. The determination
18 of accurate Eulerian (Euler) orientation angles describing each distinct 2D particle-projection is the
19 main goal of 3D refinement⁸. Once these orientations are determined, the particle views can be
20 reconstructed to produce a 3D map⁹. Ideally, the particles will be randomly oriented, hence leading to
21 an equal and uniform spread of Euler angles, yielding an isotropic map. However, in practice, uniform
22 orientation distributions are rarely observed, and non-uniform projection orientation distributions,
23 wherein one or several views of the object predominate, are ubiquitous within cryo-EM datasets¹⁰.

24

25 Non-uniformity of projection distributions is caused by the manner in which specimens are
26 vitrified on grids prior to imaging¹¹. Current grid vitrification techniques generate a thin aqueous film
27 of vitreous ice, in which protein particles are embedded. For holey grids, the two interfaces at the
28 boundary of the aqueous film attract macromolecular objects and lead to them adhering to either or
29 both interfaces and adopting “preferred orientations”. This results in over- and under-represented
30 views of the object, *i.e.* the set of projection views in the dataset and the coverage of Fourier space
31 within the reconstruction are non-uniform. In the simplest scenario, non-uniform angular projection
32 coverage leads to certain views becoming overpopulated, and in such cases the reconstructed map will
33 be characterized by directional resolution anisotropy¹², with the poorest resolution being parallel to
34 the direction of the electron beam¹³. However, in extreme cases, regions of Fourier space may be
35 entirely missing. Severe directional resolution anisotropy compromises the fidelity of features within

1 the reconstructed map, leading to ambiguities in biological interpretations (with and/or without an
2 atomic model), and potentially stifling structure elucidation efforts¹⁴.

3

4 A principal readout for directional resolution anisotropy is the 3D Fourier shell correlation (FSC)
5 volume, a variation of the conventional 1D FSC curve¹⁵. Restricting the conventional FSC to a cone
6 provides a consistency measure along a defined viewing direction, and repeating this calculation for
7 different directions generates a complete measure of directional resolution across Fourier space^{16,17}.
8 Combining 1D conical FSC curves obtained from different angular directions yields a real 3D array
9 termed the 3D FSC, which affords a quantitative assessment of the directional dependence of
10 resolution for the reconstructed object. In addition to affecting directional resolution, non-uniform
11 angular coverage also affects global resolution¹³. In the presence of non-uniform angular coverage,
12 there is a net increase in noise variance and a corresponding attenuation of the 1D FSC curve that is
13 used to define global resolution¹³. This attenuation can be estimated by a geometrical factor called the
14 Sampling Compensation Factor (SCF)^{13,14}, which derives its name from the effect of the geometry of
15 the sampling (relative to a uniform projection distribution) on the spectral signal-to-noise ratio
16 (SSNR), and by extension the FSC. As shown previously¹³, the effect of the projection distribution
17 completely decouples from other experimental issues of the collection. The SCF is defined to be the
18 harmonic mean of the sampling, over a shell of Fourier space, divided by the usual mean, and
19 therefore ranges from 0 to 1. It provides a quantitative metric for evaluating an orientation distribution.
20 Using the standard model of image formation for cryo-EM (which is used in the literature for many
21 things such as the FSC=1/7 resolution criterion), we derived that the SCF governs how much the
22 SSNR is decremented relative to a uniform distribution. The SCF for the uniform distribution
23 evaluates to the maximum value, 1, whereas an orientation distribution defined by perfect side-like
24 views, which is completely (albeit still inhomogeneously) sampled, has an SCF that evaluates to 0.81.
25 Because the side-like case, characterized by an SCF of around 0.81, represents the minimal case
26 wherein Fourier space is completely sampled, we use this value as the baseline for a good map
27 throughout the work. When there are large inhomogeneities in the sampling, the SCF rapidly
28 decrements towards zero. Cases characterized by top-like distributions, which typically arise from
29 preferentially oriented protein samples that are prevalent among experimental cryo-EM datasets, are
30 frequently attenuated by a factor of as much as ten, in comparison to the uniform distribution (*i.e.*
31 their SCFs are approaching 0.1, and even lower). In practice, reconstructions from samples
32 characterized by such orientation distributions are not only attenuated in global resolution, but also
33 characterized by severe anisotropy. Collectively, non-uniform sampling will affect directional
34 resolution anisotropy, as measured by the 3D FSC, and will also attenuate global resolution, as
35 measured by the SCF.

36

1 A simple and generalizable solution to address the effects of non-uniform sampling caused by
2 preferred orientation is to tilt the stage during data collection¹⁵. Although there are numerous possible
3 experimental procedures that will alter the behavior of the object within the vitreous ice layer, their
4 success is specimen-dependent and not generalizable (reviewed in ¹⁸). Tilting the stage offers the
5 simplest generalizable solution to the orientation bias problem. Due to the geometric configuration of
6 the preferentially oriented sample with respect to the electron beam, for each cluster of orientations,
7 tilting the stage yields a cone of illumination angles with respect to the cluster centroid, with cone half
8 angle given by the tilt¹⁵. Tilting thus spreads out the orientation distribution of the imaged object,
9 which in turn improves Fourier sampling. The quantitative benefits of tilting include a more isotropic
10 3D FSC and an SCF value that is closer to unity. Numerous successful case studies have benefited
11 from the stage-tilt approach, including samples as small as ~43 kDa¹⁹, and as large as ~100 MDa^{20,21}.

12

13 Despite the simplicity and generalizability of employing stage tilt during data collection, there
14 have been multiple drawbacks to routine implementation. First, due to doming effects²², there is
15 generally more beam-induced movement. Second, due to variations in the focus gradient, tilting can
16 lead to larger errors during image processing, for example when estimating the contrast transfer
17 function (CTF). An unavoidable drawback is the increase in ice thickness. These possible hindrances
18 lead to resolution attenuation and have historically limited the implementation of tilted data collection
19 strategies.

20

21 The main goal of this study is to evaluate the effects of tilting the stage on single-particle cryo-
22 EM reconstructions and to define optimal strategies for data collection and image analysis. Using
23 three samples differing in molecular weight and characterized by isotropic 3D FSCs, we show that the
24 quality of reconstructions derived from data collected at high stage tilt angles rivals that of the same
25 specimen collected without stage tilt. These results indicate that collecting single-particle data with a
26 fixed specimen stage-tilt on the microscope can result in negligible resolution attenuation in many
27 cases. We implement these strategies using a biological sample of bacterial RNA Polymerase (RNAP).
28 The polymerase adopts exclusively a single orientation on cryo-EM grids, making it difficult for cryo-
29 EM. We show that high-angle stage tilts, combined with our processing workflows, can overcome
30 issues with resolution anisotropy, leading to a molecular model that faithfully recapitulates the atomic
31 details of the sample.

32

33 Finally, using these observations, we devise a schema to identify an optimal tilt angle for a set of
34 orientation distributions for diverse scenarios that would be encountered by the experimentalist. The
35 presented strategies are generalizable and will guide the decision-making process of the
36 experimentalist upon initiating data collection to deal with pathologically oriented samples.

37

1

2

3 **Results**

4

5 **Experimental rationale and selection of test samples**

6

7 Resolution attenuation when tilting the specimen stage arises from at least three sources. These
8 include increases in ice thickness, larger beam-induced movement, and poorer CTF estimation.
9 Having thin ice helps with obtaining high-resolution reconstructions, because the amount of
10 inelastically and multiply scattered electrons is minimized, and there is less chance for particle
11 overlap, among other factors²³. Thus, cryo-EM practitioners frequently search for the thinnest
12 possible ice²⁴, and methods for measuring ice thickness have been developed to aid this process²⁵.
13 Beam-induced movement²⁶⁻²⁸ increases at higher tilt angles¹⁵, due to the doming effect^{22,29}, where
14 electron flux causes the ice to move up and down like a drum. Because the doming effect occurs
15 perpendicular to the plane of the grid, it becomes more pronounced during imaging when the stage is
16 tilted. The spread of defocus values corresponding to the particles may also lead to larger errors
17 during CTF estimation. Given these effects, one would expect any imaging experiment that employs
18 stage tilt to suffer from substantial resolution attenuation, and indeed these issues have limited the
19 implementation of stage tilt for single-particle data collections. However, it is clear that high-
20 resolution reconstructions can be obtained from both small¹⁹ and large^{20,21} specimens. We thus asked
21 whether and how different stage tilt angles affect high-resolution cryo-EM analysis.

22

23 We selected as test specimens several highly symmetric protein oligomers that would not suffer
24 from directional resolution anisotropy under any conditions (*i.e.* the SCF is ~1). Here, the high
25 symmetry is essential, because symmetrization of the reconstruction can naturally bring the SCF to
26 near unity, even if the specimen adheres to the air/water interface in a single orientation within the ice.
27 Thus, the resolution attenuation due to incomplete sampling¹³ is negligible and decoupled from the
28 resolution attenuation due to the detrimental effects of tilted-stage imaging. The symmetry must be at
29 minimum tetrahedral, and more preferably octahedral or icosahedral; as shown previously,
30 symmetrization of C-fold or D-fold rotationally symmetric objects may not lead to improvements in
31 sampling¹⁴, particularly with specimens for which the preferred orientation is coincident with the
32 symmetry axis relative to the direction of the electron beam. Finally, we also selected samples with a
33 range of molecular weights, because variations in particle size should approximately relate to
34 variations in the signal-to-noise ratio of individual particles.

35

1 **Resolution attenuation when the stage is tilted is negligible for large specimens such as Adeno-
2 associated virus serotype 2 capsid (AAV2)**

3

4 The first sample is AAV2³⁰, a 3.9 MDa assembly with a diameter of 250 Å. The 60-fold
5 icosahedral (T=1) symmetry of the AAV2 leads to near complete isotropic reconstructions³⁰. We
6 collected movies using the Titan Krios and the K2 direct electron detector with stage α -angle set to 0°,
7 10°, 20°, 30°, 40°, 50° or 60° (**Supplementary Table 1**). Our initial processing strategy was presented
8 previously¹⁵, also described in the Methods section. For comparative analysis, we selected an equal
9 number of 7000 particles across all tilt angles, with similar defocus spread. As expected, the resulting
10 reconstructions showed a clear trend of decreasing resolution as the tilt angle is increased (**Fig. 1a**); at
11 0° stage tilt, the resolution is 2.3 Å, but the resolution drops to 2.8 Å at 30° stage tilt, and 4.0 Å at 60°
12 stage tilt.

13

14 To improve the data processing workflow, we first tested whether recent strategies for CTF
15 estimation can improve the resolution of reconstructions generated from datasets collected using stage
16 tilt. GCTF, which we employed previously, was used as the benchmark^{15,31}. Applying the patch-based
17 CTF estimation method in cryoSPARC³² led to significant improvements in resolution for the tilted
18 data collections (**Fig. 1b**). Reconstructions from 60° stage tilt reached below 3.0 Å resolution, and
19 reconstructions from 30° stage tilt reached 2.3 Å. Notably, the reconstruction from 0° stage tilt also
20 improved by 0.1 Å to 2.2 Å. Next, we refined the CTF values against a 3D model using RELION.
21 This processing step did not improve the resolutions at lower tilt angles (0° and 10°), but did improve
22 the resolutions at higher tilt angles, e.g. from 2.9 Å to 2.5 Å for 60° (**Fig. 1c**). When combined, both
23 patch-based and per-particle refinement improved the resolution of the 60° reconstruction from 4.0 Å
24 to 2.5 Å, a cumulative 1.5 Å increase. These results indicate that accurate CTF estimations are crucial
25 to improving map quality and resolution for tilted datasets.

26

27 We next sought to account for per-particle motion, as this will help restore information lost due
28 to specimen movement during the imaging experiment^{26-28,33}. In our original report¹⁵ we used patch-
29 based motion correction, but not per-particle motion correction, such as what is currently employed in
30 RELION during Bayesian polishing³⁴. The application of RELION Bayesian polishing improved the
31 resolution of all reconstructions. For example, the 0° tilted reconstruction improved by 0.1 Å to 2.1 Å
32 resolution, while the 60° tilted reconstruction improved to 2.3 Å resolution (**Fig. 1d**). Since RELION
33 Bayesian polishing also applies an experimentally derived exposure weighting curve, the
34 improvement in resolution may also arise from this effect.

35

36 For both the CTF refinement and Bayesian polishing, the 3D map is used as a reference. A better
37 reconstruction should in turn yield more accurate CTF and particle movement parameters. Thus, we

1 sought to determine if iterative CTF refinement and Bayesian polishing can improve the resolution of
2 the tilted reconstructions. We found that the second round of CTF refinement and Bayesian polishing
3 did not improve the 0° and 10° reconstructions (both remained at 2.1 Å), but it did improve
4 reconstructions derived from data collected at higher tilt angles (**Fig. 1e-f**). No further improvements
5 were observed with the third round of CTF refinement (**Fig. 1g**). Collectively, after several iterations,
6 reconstructions from data collected at 20°–50° stage tilt reached identical resolution compared to
7 reconstructions from data collected using 0° or 10° stage tilt. The resolution of the reconstruction
8 from data collected at 60° stage tilt was just 0.1 Å less than the resolution of all other reconstructions.
9 For completeness, we applied Ewald sphere curvature correction to the reconstructions³⁰, but
10 observed no significant change in resolution (**Fig. 1h**). Higher order aberration corrections also did
11 not improve the resolution, likely because the calculated beam tilt was minimal at under 0.1 mrad.
12 These results show that, for large particles like AAV2, improved data processing strategies can
13 largely counter resolution attenuation caused by the imaging experiment when using stage tilt.

14

15 To validate the reconstructions, we compared the results from individual processing steps for
16 data collected at 0° (**Fig. 2 Left**), 30° (**Fig. 2 Middle**), or 60° (**Fig. 2 Right**). First, we noted that the
17 particles were not overly crowded in the raw images even at high-angle tilts, and high-resolution
18 features were present in all sets of 2D class averages (**Fig. 2a**). As expected, the Euler angle
19 distributions changed when the sample was tilted (**Fig. 2b**). However, the SCF remained ~1.0, and the
20 3D FSC was largely unchanged, irrespective of angular distribution and tilt angle, as expected from
21 the icosahedral symmetry (**Fig. 2c**). Importantly, the global resolution estimate measured for the map-
22 to-model FSCs matched the global resolution estimate measured for the half-map FSCs (**Fig. 2d**).
23 Finally, the experimental reconstructions showed clear side chain density and the presence of water
24 molecules with the same level of detail (**Fig. 2e**). These observations confirm that the quality of the
25 2.2 Å resolution reconstruction derived from data collected using 60° stage tilt is nearly identical to
26 that of the 2.1 Å resolution reconstruction derived from data collected using 0° stage tilt.

27

28 **Resolution attenuation at moderate tilt angle is negligible for medium-sized specimens such as** 29 **apo ferritin**

30

31 Smaller proteins scatter fewer electrons and produce less signal within cryo-EM datasets. To
32 determine if the trends for AAV2 hold for proteins of lower molecular weight, we repeated our
33 experiments using the medium-sized protein, apo ferritin³⁵, a 510 kDa multimeric assembly with
34 octahedral symmetry and diameter of ~130 Å. Using a similar data collection and processing strategy
35 as employed with AAV2 (**Supplementary Table 2** and Methods), we found that our data processing
36 workflow (patch CTF estimation, per-particle CTF refinement, and Bayesian polishing) significantly
37 improved the resolutions of reconstructions across all tilt angles (**Fig. 3**): from 2.6 Å to 2.4 Å for 0°

1 tilt data, from 3.1 Å to 2.5 Å for 30° tilt data, and from 3.8 Å to 2.7 Å for 60° tilt data (**Fig. 3a-d**). As
2 with AAV2, we observed further improvements after the 2nd round of CTF refinement and Bayesian
3 polishing (**Fig. 3e-f**), but not with the 3rd round (**Fig. 3g**). Finally, we noted small improvements when
4 correcting for higher-order optical aberrations, yielding final resolutions of 2.2 Å, 2.3 Å, and 2.5 Å
5 for reconstructions from 0°, 30°-tilted, and 60°-tilted data, respectively (**Fig. 3h**).
6

7 With these improvements, we found that the resolution attenuation at moderate tilt angles of 30°
8 was negligible compared to 0°, with both these tilt angles for data collection producing maps at a
9 nominal 2.2 Å resolution. For reconstructions from 0° (**Fig. 4, left**), 30°-tilted (**Fig. 4, center**), and
10 60°-tilted (**Fig. 4, right**) data, map features were observed in raw particles and 2D class averages (**Fig.**
11 **4a**). Although the angular distributions became increasingly dispersed (**Fig. 4b**), this dispersion was
12 largely inconsequential to the sampling distribution or the 3D FSC (**Fig. 4c**). The derived
13 experimental resolution was corroborated via similar half-map and map-to-model resolutions (**Fig. 4d**)
14 and nearly identical looking density maps, with features that correspond to the expected nominal
15 resolution (**Fig. 4e**).
16

17 In support of and consistent with the above findings, in early experimental attempts with
18 apoferritin as a test specimen, we collected data with the stage α -angle set to 0° or 30°, *i.e.* omitting
19 the other angles. After image processing, we were able to resolve maps to nearly identical 1.9 Å for
20 reconstructions from both 0° data and 30°-tilted data (**Supplementary Table 3** and **Supplementary**
21 **Fig. 1**). The higher resolution for these maps, in comparison to the maps described above, can be
22 attributed to the larger data size. In yet another set of experiments, we employed the ~700 kDa 20S
23 proteasome, which is characterized by D7 symmetry but has a non-uniform orientation distribution
24 due to the side-like sampling of particle views. We collected cryo-EM data with the stage α -angle set
25 to 0°, 10°, 20°, 30°, 40°, 50°, but omitted a dataset employing 60° stage tilt (**Supplementary Table 4**).
26 After image processing, we observed similar trends as with apoferritin (**Supplementary Fig. 2-3**).
27

28 Collectively, reconstructions from 0° data and as high as 50°-tilted data were largely similar.
29 However, when the stage α -angle was increased to 60°, the resolution of the apoferritin reconstruction
30 was ~0.3 Å poorer compared to the others. It is possible that workflow optimization may yield further
31 resolution gains, especially with future improvements in hardware/software, but we were not able
32 accomplish this using current strategies. The ancillary data in which the complete tilt series was not
33 collected were fully supportive of our main findings. We conclude that resolution attenuation is
34 largely negligible for medium-sized specimens, except for the highest tilt angles.
35

1 **Resolution is attenuated with increasing stage tilts for small specimens such as DNA protection
2 during starvation protein (DPS)**

3

4 We next turned our attention to our smallest specimen, the 230 kDa DPS³⁶, which is
5 characterized by tetrahedral symmetry. We again collected datasets with the stage α -angle set to 0° or
6 tilted up to 60°, in 10° increments (**Supplementary Table 5**). As with the larger protein specimens,
7 we observed most of the improvements in resolution after one round of patch CTF estimation and
8 Bayesian polishing (**Fig. 5a-d**). However, CTF refinement before and after Bayesian polishing did not
9 improve the resolution, likely because of the low signal-to-noise ratio for the smaller DPS particles.
10 We observed only minor resolution changes in the second round of Bayesian polishing and final CTF
11 refinement (**Fig. 5e-f**), and no further changes afterwards (**Fig. 5g**). Correcting for higher-order
12 aberrations yielded small gains (**Fig. 5g**). Although tilting the stage produced a slightly poorer
13 reconstruction for DPS compared to the reconstruction when the stage was not tilted, our revised data-
14 processing workflow again yielded significant improvements in resolution for reconstructions across
15 all tilt angles – from 3.0 Å to 2.6 Å for 0°; from 3.6 Å to 3.0 Å for 30°; and from 4.4 Å to 3.3 Å for
16 60°. All the metrics for evaluating map quality were consistent with the reported nominal resolution
17 values (**Fig. 6a-d**). Importantly, our results show that with appropriate data processing, tilting the
18 stage is a viable strategy to obtain high-resolution reconstructions even for small proteins suffering
19 from preferred orientation. This in turn will allow for accurate derivation of atomic models, as
20 evidenced by the final quality of the experimental maps (**Fig. 6e**). As specimen preparation, hardware,
21 and data-processing algorithms advance, we expect that resolution attenuation will accordingly
22 diminish in the future.

23

24 **High-angle stage tilt addresses the orientation bias problem in RNAP**

25

26 We then used the *E. coli* RNAP to evaluate the generalizability of our tilted-stage image
27 acquisition. This is especially challenging for RNAP, which is known to exhibit strong preferential
28 orientation on cryo-EM grids³⁷; conventional data collection strategies have typically yielded maps
29 characterized by severe resolution anisotropy characterized by elongated features. The inclusion of
30 detergent can produce additional views³⁷, leading to resolvable features within cryo-EM maps,
31 however, the resulting orientation distribution remains non-uniform. Further, it is well-known that the
32 addition of detergent is not a generalizable strategy to address preferential orientation for other
33 protein assemblies. The overall molecular weight is approximately 480 kDa, which is comparable to
34 apoferritin. But RNAP lacks internal symmetry, which precludes mitigating the effects of directional
35 resolution anisotropy.

36

1 To confirm prior observations, we collected several tilt series from a grid used for single-particle
2 analysis. In the resulting tomograms, almost all particles reside at either one of the two air/water
3 interfaces (**Fig. 7** and **Supplementary Movie 1**) and thus are not randomly oriented within vitreous
4 ice.

5

6 We began by collecting a dataset for RNAP with the stage α -angle set to 0° and obtained a map
7 nominally resolved to $\sim 3.7 \text{ \AA}$ (**Supplementary Table 6**). However, this map suffered from severe
8 directional resolution anisotropy and was characterized by an SCF of ~ 0.4 . To determine an optimal
9 tilt angle for data collection, we used the sampling tool we developed that was previously extended to
10 the community, which determines, based on the SCF of the reconstruction from untilted data, how the
11 orientation distribution (and by extension, the resulting SCF) can improve when the stage is tilted^{13,14}.
12 We predicted that a 51° tilt-angle should yield an orientation distribution characterized by an SCF of
13 ~ 0.81 , which would result in a fully sampled reconstruction. From a dataset collected with the stage
14 α -angle set to 51° , we obtained reconstructed maps from heterogeneous refinement that were
15 characterized by a sampling distribution with a mean SCF of ~ 0.7 (**Supplementary Table 6** and
16 **Supplemental Fig. 4**) and substantially less anisotropy than the reconstructed map from the untilted
17 data. The discrepancy between the predicted SCF of 0.81 and the experimentally measured SCF of
18 0.7 from data collected at the predicted optimal 51° tilt-angle can be attributed to angular mis-
19 assignment of particles within the untilted dataset. The erroneous inclusion of a small amount of
20 false-positive projections would yield overly optimistic SCF values for the untilted orientation
21 distribution, which would in turn translate to an underestimate of the predicted optimal tilt angle, as
22 further explained in the Discussion section. Thus, we increased the stage α -angle to 60° , which is the
23 maximum amount of stage tilt that can be set on most electron microscopes, and collected a dataset
24 (**Supplementary Table 6**). We calculated independent reconstructions from a subset of 72,000
25 particles with each of the 0° and 60° -tilted datasets. Analogous to the symmetric particles, we
26 obtained iterative improvements in resolution with the updated processing approaches for
27 reconstructions from 60° -tilted data (**Supplementary Fig. 5**). For reasons that are explained in
28 **Supplementary Note 1**, the improvements in global resolution for RNAP reconstructions obtained
29 from 0° data are not reliable and cannot be compared with the 60° -tilted data.

30

31 We next evaluated comparatively the RNAP cryo-EM maps using the standardized metrics. Raw
32 particles could readily be observed for both 0° data and 60° -tilted data, but as expected, the 2D
33 averages were consistent with distinct sets of views (**Fig. 8a**). Typical of a preferentially-oriented
34 sample with C1 symmetry, for RNAP only one clear orientation was evident, with a narrow Euler
35 angle distribution (**Fig. 8b, left**); when the stage was tilted, the distribution became conical with
36 respect to the cluster centroid, with cone half angle given by the tilt (**Fig. 8b, right**). The

1 reconstruction from untilted data hyper-sampled the region of Fourier space in and around a single
2 plane and had a characteristically low SCF value (**Fig. 8c, left**), but the sampling improved when the
3 stage was tilted, and the SCF was higher (**Fig. 8c, right**). As described previously¹⁵, we observed a
4 large discrepancy between the half-map and map-to-model FSCs for the reconstruction from 0° data
5 (**Fig 8d, left**); the half-map and map-to-model FSCs were more similar for the reconstruction from
6 60°-tilted data (**Fig. 8d, right**). Most importantly, significant qualitative differences between the
7 reconstructed maps were clearly evident. With the reconstruction from 0° data, the features of the map
8 were severely elongated, and it was nearly impossible to fit, or properly interpret, an atomic model
9 from the density (**Fig. 9a top**). In stark contrast, the reconstruction from 60°-tilted data produced a
10 map with features fully consistent with the model (**Fig. 9a bottom**). This latter map was comparable
11 in quality to typical reconstructions derived using cryo-EM^{37,38} and readily lent itself to biological
12 interpretations.

13

14 Based on the model derived from the density, we are able to reveal important features of *E. coli*
15 RNAP elongation complexes. These include base stacking of upstream RNA:DNA hybrid and side
16 chains of conserved structural motifs, such as bridge helix (**Fig. 9b**).

17

18 **Geometric and sampling considerations for defining an optimal tilt angle for various orientation
19 distributions**

20

21 To help guide users in defining an optimal tilt angle for data collection, we sought to provide a
22 comprehensive and quantitative analysis of how different orientation distributions affect the SCF. We
23 performed calculations according to two distinct scenarios, distinguished by the nature of the particle
24 orientation distributions. The first scenario was characterized by a single conical distribution, wherein
25 projections were constrained within a single cone defined by a half-angle of either 15°, 30°, 45°, or 60°
26 degrees. This scenario simulates the case in which there is only one preferential orientation of the
27 specimen. The second scenario was identical, except that we added a second set of projections,
28 orthogonal to the first and characterized by an identical conical distribution. This scenario simulates
29 the case in which there are two preferential orientations, related orthogonally to one another. To the
30 orientation distribution for each of these scenarios, we then added randomly “sprinkled” projections
31 outside of the primary conical orientation distribution. These sprinkled projections simulate the
32 scenario in which a small subset of particles may reside within the ice layer, *i.e.* in between the two
33 air-water interfaces, and are therefore free to adopt any orientation. For each scenario, we then
34 simulated a series of data collections with a nominal stage tilt ranging from 10° to 60°, in 10°
35 increments. We derived SCFs for all subsets, and we present the results in **Fig. 10**.

36

1 We first examined the most pathological scenario, wherein the projection distribution is narrowly
2 confined to a cone of 15° (**Fig. 10a**). For such a distribution, the SCF is <0.81 in nearly all cases
3 without remedial data-collection protocols. A 60° stage tilt, coupled with at least 20% sprinkled
4 projections, is minimally required to yield a fully sampled reconstruction characterized by an SCF of
5 at least 0.81. A lower stage tilt angle can be applied only if there are many projections randomly
6 distributed outside of the primary projection cone. Next, if the orientations are distributed within a 30°
7 cone, then applying a 60° stage tilt will lead to a fully sampled reconstruction, irrespective of the
8 number of sprinkled projections. A smaller stage tilt can be applied, but the number of sprinkled
9 projections outside of the main conical distribution must be at least 10% if a 50° stage tilt is used, and
10 higher for smaller stage tilt angles. With a conical distribution of 45°, the application of a 50° stage
11 tilt will now yield a fully sampled map. Furthermore, a smaller tilt angle can be used, such as 40° or
12 even 30°, if a small amount of particle projections is sprinkled. Finally, if the projections are
13 constrained to a 60° cone, the application of a 30° stage tilt will yield a fully sampled map, and
14 smaller angles can be readily applied, depending on the number of sprinkled projections.
15

16 In the second scenario, representative of a sample possessing two orthogonally related conical
17 distributions, the situation is considerably improved (**Fig. 10b**). Given a conical-distribution of 15°, a
18 tilt angle of 40° will yield a fully sampled map, and in practice, a stage tilt angle of 30° can be used
19 for most applications if even a small number of particles are oriented randomly outside of the two
20 main distributions. With a 30° conical-distribution, the requisite tilt angle drops to 30°. Finally, for
21 orthogonally populated sets with both 45°- and 60°- positioned distributions, tilting the stage is
22 largely unnecessary, because both sets of distributions lead to fully (or nearly fully) sampled
23 reconstructions, irrespective of the number of sprinkled projections.
24

25 **Discussion**

26

27 In this work, using novel data processing methods, we extended the resolution of reconstructions
28 from micrographs collected using stage tilt, to the point at which the maps derived from data collected
29 with or without stage tilt are virtually indistinguishable. The improvement in global resolution is due
30 to novel and iterative methods for refining CTF parameters and correcting for beam-induced motion.
31 Although it is not practical to evaluate all available algorithms for data analysis, we envision that
32 there are additional methodologies that can further extend the resolution of reconstructions from tilted
33 images, and undoubtedly future advances will lead to even greater improvements.
34

35 When the stage is tilted, the amount of ice that the beam traverses become increasingly large as
36 the tilt angle progresses towards 90°, because the effective ice thickness varies as $1/\cos(\text{tilt})$. At 30°

1 stage tilt, the ice is thicker by ~15%, but at 60° stage tilt, the ice is thicker by 100% (*i.e.* twice). For
2 higher tilt angles (~ $\geq 40^\circ$), the particle density in a given field of view may need to be optimized,
3 because the effective projection area of a hole is reduced. This can be achieved by selecting areas
4 containing more sparsely dispersed particles, such that when the stage is tilted, particles do not
5 overlap. Thicker ice will lead to an increase in inelastic scattering that can only be partially corrected
6 using energy filters²⁵. Experimentally, the limits of ice thickness have recently been explored for
7 single-particle cryo-EM reconstructions by Neselu *et al.* using apoferritin as a test system³⁹. They
8 showed that even with ice thickness ranging between 200-500 nm, it was possible to obtain a sub-3 Å
9 reconstruction, although an energy filter and an acceleration voltage of 300 keV were both necessary.
10 In the absence of an energy filter, the ice needed to be ~100-150 nm to yield sub-3 Å reconstructions.
11 Independently, ice thickness limits for micro-electron diffraction have also been evaluated, with ice
12 thickness of up to 360 nm showing no significant resolution loss for the resolution limit of around 2
13 Å⁴⁰. Because most purified samples used for single-particle cryo-EM are characterized by ice that is
14 less than ~100 nm in thickness³⁹, we suggest that ice thickness, *per se*, may not inherently limit the
15 resolution. The more important consideration is whether the SNR for particles embedded within the
16 ice layer is sufficient to assign correct orientations, as described below.

17
18 As the stage tilt angle is increased, beam induced motion becomes progressively larger,
19 especially in the first few movie frames of data acquisition. Because the first ~2-5 e-/Å² carry the
20 most high-resolution information, it is important to design the data collection and processing schemes
21 so as to maximize the information from the experiment. It is possible to reduce beam-induced motion
22 by using gold substrate grids³⁵ and to computationally correct for residual beam-induced motion
23 recorded within the movies^{34,41-43}. A combination of these two techniques may be necessary to
24 overcome a large amount of cumulative motion, especially within the initial frames of the recorded
25 movies. Although these steps have become routine even for standard untilted data collection, they are
26 especially important for data collection schemes that employ stage tilting.

27
28 During computational data analysis, the defocus values for each particle are not known *a priori*
29 and must be estimated from the data^{18,44}. The closer the estimate is to the true defocus value, the better
30 the correction, and hence the higher the resolution of the reconstruction⁴⁵. In the absence of stage tilt,
31 the defocus values for particles have a small spread. However, when the grid is tilted, there is a focus
32 gradient in the field of view in addition to variations in focus due to the particle positions. Variations
33 in focus in the image could be estimated using local CTF estimation approaches, but these typically
34 rely on smaller regions of the image; the smaller fields of view may give rise to increased error in the
35 estimates. There are numerous novel algorithms^{31,46-50} that have led to improvements to the accuracy
36 of local CTF estimation. In our experience working with different datasets, all the newer software
37 implementations have yielded improvements to the final resolution estimates of both untilted and

1 tilted datasets. As shown here, the improvements to resolution are particularly pronounced for tilted
2 datasets (**Fig. 1, 3, 5**, and **Supplementary Fig. 2 and 5**). While we demonstrate one specific
3 workflow in our current approach that employs the RELION and cryoSPARC softwares, there are
4 likely alternative approaches that can yield similar improvements.
5

6 We did not attempt to quantify or evaluate the resolution attenuation associated with every
7 possible parameter for data collection and/or image processing, because we view this as a moving
8 target. As the methods improve and the field matures, the attenuation will become smaller. Ultimately,
9 the experimentalist cares about the signal-to-noise ratio (SNR) of the final particle images, and how a
10 drop in SNR can affect one's ability to refine a map reconstruction. The larger the particle, the higher
11 the SNR, and the less resolution attenuation there will be as the stage is tilted. It seems that for a
12 particle the size of AAV2, the decrease in SNR is not sufficient to impact the ability to align particles
13 to significantly attenuate resolution for maps resolved to ~2 Å, even at tilt angles as high as 60° (**Fig.**
14 **1-2**). Of note, our AAV2 data was collected using the previous generation K2 Summit direct electron
15 detector, whereas newer detectors, such as the K3 or Falcon4, have improved detective quantum
16 efficiencies and allow the experimentalist to use higher frame rates to correct for beam-induced
17 movement. For particles the size of apoferritin, the data processing strategies that we have employed
18 are, in most cases (except for the 60° tilt angle) sufficient to obtain global resolutions for tilted
19 datasets that are similar to or nearly indistinguishable from their respective untilted counterparts (**Fig.**
20 **3-4**). Moreover, we show that sub-2 Å resolution reconstructions are attainable from 30°-tilted images,
21 and this reconstruction is virtually indistinguishable from a reconstruction from untilted images
22 (**Supplementary Fig. 1**). For smaller proteins, tilting the stage apparently leads to more information
23 loss, because there is a drop in relative SNR of the particles. Current methods may not fully recover
24 high-resolution features in comparison to reconstructions from untilted data collections (**Fig. 5-6**).
25 Nevertheless, stage tilt has been employed for proteins as small at ~43 kDa to improve map quality⁵¹.
26 Possible methods to improve the SNR of images containing small proteins include: the use of
27 denoising algorithms to boost the low to intermediate resolution spatial frequency ranges^{52,53}, and thus
28 facilitate orientation alignment; the use of electron detectors with better DQE; the use of novel grid
29 substrates, such as HexAufoil⁵⁴. In the case of HexAufoil grids, even when the stage is tilted, the
30 apparent root mean square displacement of specimen motion is comparable to untilted data
31 collection⁵⁴. These strategies, along with the data processing pipeline described here, may be required
32 for tilted data collection of smaller proteins suffering from pathological preferred orientation.
33

34 We applied our methods to the structure determination of RNAP (**Fig. 8-9**). In the reconstruction,
35 we could clearly resolve important features of the RNAP elongation complex, such as base stacking
36 of upstream RNA:DNA hybrid, and the side chains of the bridge helix.
37

1 Finally, we demonstrate a practical framework for quantifying the amount of stage tilt that would
2 be required to overcome resolution anisotropy inherent to preferentially oriented specimens (**Fig. 10**).
3 The SCF values derived from varying *(i)* the cone size of the projection distribution, *(ii)* the number
4 of sprinkled projections outside the cone, or *(iii)* the tilt angle applied to the dataset, are consistent
5 with experiment, as evidenced using the dataset of RNAP. In the absence of stage tilt, the orientations
6 for RNAP are distributed within a cone of ~20-25°, with a small number of sprinkled projections. We
7 found that collecting data with the stage tilt angle set to 60° led to a nearly, but still incompletely
8 sampled reconstruction, characterized by an SCF of 0.78. The fact that the SCF was just shy of the
9 suggested baseline of 0.81 means that the primary projection distribution is <30° and there are few
10 true positive orientations outside of the primary projection distribution. Our initial predicted optimal
11 stage tilt angle was 51°, which should have led to an orientation distribution characterized by an SCF
12 of 0.81. In practice, we found that a slightly higher stage tilt angle was necessary to yield a (nearly)
13 fully sampled map. Importantly, the features of the map from data collected at 60° stage tilt were of
14 high-quality, allowing us to derive an accurate atomic model and highlight novel aspects of RNAP
15 biology. We attribute the overly optimistic initial SCF prediction to the inclusion of extraneous false-
16 positive angular orientation assignments. Currently, there are no effective methods to quantify or
17 eliminate false-positive angular assignments in cryo-EM data, and hence the user is advised to apply a
18 slightly higher tilt angle than what is predicted. Collectively, these results provide a quantitative,
19 graphical representation for the SCF of cryo-EM reconstructions. Our SCF analyses will help users
20 define an optimal tilt angle for any dataset characterized by preferred orientation.

21
22

1 **Acknowledgements**

2

3 We would like to thank the late Dr. Mavis Agbandje-McKenna for her pioneering studies of
4 parvovirus capsid structures. We thank Chris Russo for the plasmid for DPS, and Yifan Cheng for the
5 20S proteasome sample. We thank Nikolaus Grigorieff, Timothy Grant, Alexis Rohou, Anchi Cheng,
6 Alex Noble, Bridget Carragher, and Clinton S. Potter for their invaluable advice. We thank Bill
7 Anderson at TSRI for help with microscope maintenance, Laura Yen at NYSBC for assistance with
8 freezing grids and single-particle data collection of the 20S proteasome, and Craig K. Yoshioka at
9 PNCC for assistance with tomography data collection. Molecular graphics and analyses performed
10 with UCSF ChimeraX, developed by the Resource for Biocomputing, Visualization, and Informatics
11 at the University of California, San Francisco, with support from National Institutes of Health R01-
12 GM129325 and the Office of Cyber Infrastructure and Computational Biology, National Institute of
13 Allergy and Infectious Diseases. The work was supported by National Institutes of Health (U54
14 AI170855 and U01 AI136680 to D.L., GM148476 to D.W., GM082946 to R.M. and M.A.) the
15 National Science Foundation (MCB 2048095 to D.L.); Hearst Foundations Developmental Chair and
16 the Margaret T. Morris Foundation (to D.L.); National University of Singapore (A-0008405-00-00,
17 A-0008405-01-00 to Y.Z.T.); Ministry of Education Singapore (A-8000037-00-00 to Y.Z.T.);
18 National Research Foundation Singapore (A-8001346-00-00 to Y.Z.T.); Agency for Science,
19 Technology and Research Singapore (to Y.Z.T.). D.A.G. is supported by the Nadia's Gift Foundation
20 Innovator Award of the Damon Runyon Cancer Foundation (DRR-65-21). B.A.B is supported by an
21 American Cancer Society postdoctoral fellowship (PF-21-075-01-CCB). Some of the work was
22 performed at the National Resource for Automated Molecular Microscopy at the Simons Electron
23 Microscopy Center which is supported by National Institute of General Medical Sciences
24 (GM103310), Simons Foundation (SF349247), and NYSTAR. The cryo-EM data was collected at
25 Scripps Research (supported by S10 OD032467), New York Structural Biology Center, and Janelia
26 Research Campus. S.H. and S.A.B., and the development of unnatural base pairs were supported by
27 the National Science Foundation under Grant MCB-1939086.

28

29 **Author Contributions**

30

31 D.L. and Y.Z.T. conceived the project. M.M. and J.A.H. purified AAV2 under supervision of R.M.
32 and M.A. M.E.B. and G.L. expressed and purified DPS under J.A.P.N.'s supervision. J.O. purified
33 RNAP under D.W.'s supervision. S.H. made the artificial bases under S.A.B.'s supervision. S.D.M.
34 and S.A. prepared apo ferritin samples for data collection at Scripps Research. D.P. prepared
35 apo ferritin samples for data collection at Janelia Research Campus and S.A. collected and processed

1 the cryo-EM data collected at Scripps Research and Janelia Research Campus. S.A. froze the grids for
2 DPS, and Y.Z.T. collected the cryo-EM data. S.A. froze the RNAP grids and collected the cryo-EM
3 data. Y.Z.T. collected the proteasome cryo-EM data. S.A., S.M.T., and Y.Z.T. processed the cryo-EM
4 data. Z.S. and J.O. built and refined the model for RNAP. P.R.B. performed the SCF calculations.
5 A.M collected, processed, and analyzed RNAP tomography data with B.A.B, D.A.G and D.L
6 providing guidance and supervision. R.M., M.A.M., J.A.P.N., D.W. and D.L. provided funding
7 support. S.A., P.R.B., Y.Z.T. and D.L. wrote the manuscript, with input from all co-authors.
8

9 **Competing Financial Interests**

10
11 The authors declare no financial conflict of interest.
12

13

1 **Figure Legends**

2

3 **Figure 1 | Improvement in resolution for AAV2 at different tilt angles.** AAV2 cryo-EM data was
4 collected at increasing stage tilt angles (0° , 10° , 20° , 30° , 40° , 50° , 60°) and equalized for defocus,
5 with 7,000 particles used per tilt angle. The particles were processed using an identical workflow. (a)
6 baseline processing strategy presented in Tan et al¹⁵. (b to h) Individual steps were added to the
7 workflow, and improvements in resolution are plotted as lines. These include (b) patch-based CTF
8 estimation in cryoSPARC, (c) CTF refinement in RELION, (d) Bayesian polishing in RELION, (e) a
9 second round of CTF refinement and (f) Bayesian polishing, (g) a third round of CTF refinement, and
10 (h) Ewald curvature correction.

11

12 **Figure 2 | Evaluation metrics for AAV2 at representative tilt angles.** Evaluation metrics of the
13 cryo-EM data and reconstructed maps for the processing strategy outlined in Fig. 1. Results for
14 untilted (left column), 30° -tilt (middle column) and 60° -tilt (right column) are compared. (a)
15 Micrographs at $1.0\text{ }\mu\text{m}$ defocus, with corresponding 2D class averages at right. (b) Final Euler angle
16 distribution. (c) Surface sampling plot with the SCF value below (left) and central slice through the
17 3DFSC, coloured by resolution (right). (d) Half-map and map-to-model global FSC curves. (e) Map
18 density with docked atomic model.

19

20 **Figure 3 | Improvement in resolution for apo ferritin at different tilt angles.** Apoferritin cryo-EM
21 data was collected at increasing stage tilt angles (0° , 10° , 20° , 30° , 40° , 50° , 60°) and equalized for
22 defocus, with 17,000 particles used per tilt angle. This figure follows the format of Fig. 1. The
23 particles were processed using an identical workflow. (a) baseline processing strategy used in Tan et
24 al¹⁵. (b to h) Individual steps were added to the workflow and improvements in resolution are plotted
25 as lines.

26

27 **Figure 4 | Evaluation metrics for apo ferritin at representative tilt angles.** Evaluation metrics of the
28 cryo-EM data and reconstructed maps for the processing strategy outlined in Fig. 3. Results for
29 untilted (left column), 30° -tilt (middle column) and 60° -tilt (right column) are compared. (a)
30 Micrographs at $1.3\text{ }\mu\text{m}$ defocus, with corresponding 2D class averages at right. (b) Final Euler angle
31 distribution. (c) Surface sampling plot with the SCF value below (left) and central slice through the
32 3DFSC, coloured by resolution (right). (d) Half-map and map-to-model global FSC curves. (e) Map
33 density with docked atomic model.

34

35 **Figure 5 | Improvement in resolution for DPS at different tilt angles.** DPS cryo-EM data was
36 collected at increasing stage tilt angles (0° , 10° , 20° , 30° , 40° , 50° , 60°) and equalized for defocus,

1 with 1,750 particles used per tilt angle. This figure follows the format of **Fig. 1**. The particles were
2 processed using an identical workflow. **(a)** baseline processing strategy used in Tan et al¹⁵. **(b to f)**
3 Individual steps were added to the workflow and improvements in resolution are plotted as lines.
4

5 **Figure 6 | Evaluation metrics for DPS at representative tilt angles.** Evaluation metrics of the cryo-
6 EM data and reconstructed maps for the processing strategy outlined in **Fig. 5**. Results for untilted
7 (left column), 30°-tilt (middle column) and 60°-tilt (right column) are compared. **(a)** Micrographs at
8 1.3 μm defocus, with corresponding 2D class averages at right. **(b)** Final Euler angle distribution. **(c)**
9 Surface sampling plot with the SCF value below (left) and central slice through the 3DFSC coloured
10 by resolution (right). **(d)** Half-map and map-to-model global FSC curves. **(e)** Map density with
11 docked atomic model.
12

13 **Figure 7 | Tomographic reconstruction of a tilt-series showing RNAP particles at the air-water**
14 **interface.** **(a)** Representative slice through a tomogram showing the hole used for imaging (left) and
15 rendering of particles within the same reconstructed tomogram viewed down the XY plane (right). **(b)**
16 Cross-sectional view of the tomogram along entirety of the YZ plane. **(c)** Thin slices of cross-
17 sectional views at 3 distinct locations along the YZ-plane, with the top, middle and bottom slices
18 representing three distinct locations of the hole. Dashed boxes in panel (a) display the locations of
19 each slice in panel (c).. Particles are coloured according to their positions along the Z-axis, as
20 extracted from the metadata file. Color key is described by the scale at the bottom-right panel.
21

22 **Figure 8 | Evaluation metrics for RNAP at 0° and 60° tilt angles.** RNAP data was collected
23 without tilts and at 60° tilt angle. **(a)** Micrographs at 1.3 μm defocus, with corresponding 2D class
24 averages at right. **(b)** Final Euler angle distributions. **(c)** Surface sampling plots with the SCF value
25 below (left) and central slice through 3DFSC, coloured by resolution. **(d)** Half-map and map-to-model
26 global FSC curves.
27

28 **Figure 9 | Map and model of RNAP.** **(a)** RNAP maps from data collected without tilt (top) and with
29 60°-tilt (bottom) are shown, with (right) and without (left) the superimposed atomic model. The map
30 features from the reconstruction from 0° data are elongated and cannot be properly interpreted with an
31 atomic model. In contrast, the map features from the reconstruction from 60° data are consistent with
32 the expected densities for the chemical groups. **(b)** Map features that of RNAP that can be clearly
33 observed within the reconstructions from 60° tilted data include the bridge helix, the trigger loop and
34 the RNA:DNA hybrid.
35

36 **Figure 10 | Quantitative assessment of how tilting improves Fourier sampling.** The value of the
37 SCF is calculated for datasets **(a)** either with a single preferred orientation (schematic on top right) or

1 **(b)** two preferred orientations orthogonal to another (schematic on top right). The SCF for a given tilt
2 angle is calculated as a function of both the percentage of other views (sprinkles) and the spread of
3 the preferred orientation (cone half angle). The SCF value range is displayed from 0.0 (red) to 1.0
4 (blue) (bottom right in both panels **a** and **b**).
5
6

1 **Supplementary Note 1**

2

3 For reconstructions from 0° data, the Fourier shell correlation curves indicated that the map was
4 initially resolved to nominal resolution of 3.7 Å. This resolution improved to 3.1 Å after
5 implementing the Bayesian polishing routine, but then worsened to and stabilized at 3.4 Å in
6 subsequent stages of processing. The fluctuations in resolution (**Supplementary Fig. 5**) indicate
7 several issues: the nominal resolution values of ~3–4 Å are inconsistent with the features evident
8 within the maps; the fluctuations in nominal resolution are inconsistent with the more systematic
9 improvements that we observe in all other datasets, and with the expected behavior of refinement
10 protocols. We attribute these inconsistencies to the pathologically preferential orientation distribution
11 of RNAP, and as a result, to missing data in the reconstructed map. As previously shown, a single
12 top-like orientation distribution for a particle leads to heavily undersampled and/or missing data in
13 Fourier space within the reconstruction¹³. This undersampling is present in both half-maps that are
14 used to compute the FSC and the voxels may be correlated and reinforced during refinement, skewing
15 the calculation of the global FSC. There is also a second possible issue that was previously
16 described¹³, wherein the FSC curve becomes inflated if there are zeros present in the transform, e.g.
17 due to missing or sparsely assigned orientations (in practice, we do not know whether the orientations
18 assigned into sparsely populated regions of Euler space are true positives). For these reasons, in cases
19 characterized by severe preferred orientation, the global half-map FSC may not be useful in judging
20 the improvement in map quality.

21

22

23

1 **Supplementary Figure 1 | High resolution reconstruction of apoferritin from 0° and 30° tilts.**

2 Using the updated processing strategy, apoferritin was collected without tilts and with a 30° stage tilt
3 and equalized for defocus, with 64,000 particles used per tilt angle. **(a)** The micrographs at 1.1 μm
4 defocus, 2D class averages, **(b)** final Euler angle distribution, SCF plot, **(c)** 3DFSC slice, **(d)** map-to-
5 map and map-to-model FSC, and **(e)** map density with docked model are displayed for untilted (left)
6 and 30° tilted (right) reconstructions.

7

8 **Supplementary Figure 2 | Improvement in resolution for the 20S proteasome at different tilt**
9 **angles.** The 20S proteasome cryo-EM data was collected at increasing stage tilt angles (0°, 10°, 20°,
10 30°, 40°, 50°) and equalized for defocus, with 5,000 particles used per tilt angle. This figure follows
11 the format of **Fig. 1**. The particles were processed using an identical workflow. **(a)** baseline
12 processing strategy used in Tan et al¹⁵. **(b to e)** Individual steps were added to the workflow and
13 improvements in resolution are plotted as lines. No further improvements were observed after the 2nd
14 round of CTF refinement.

15

16 **Supplementary Figure 3 | Evaluation metrics for the 20S proteasome at representative tilt**
17 **angles.** Evaluation metrics of the cryo-EM data and reconstructed maps for the processing strategy
18 outlined in **Supplementary Fig. 2**. Results for untilted (left column), 30°-tilt (middle column) and
19 50°-tilt (right column) are compared. **(a)** Micrographs at 2 μm defocus, with corresponding 2D class
20 averages at right. **(b)** Final Euler angle distribution. **(c)** Surface sampling plot with the SCF value
21 below (left) and central slice through 3DFSC (right), coloured by resolution. **(d)** Half-map and map-
22 to-model global FSC curves. **(e)** Map density with docked atomic model.

23

24 **Supplementary Figure 4 | Cryo-EM maps derived from data collected at 51° stage tilt angle for**
25 **RNAP.** 85,340 particles are classified into 3 classes using Heterogeneous refinement in cryoSPARC,
26 with 29,913 particles in class 1, 28,205 particles in class 2, and 27,222 particles in class 3. **(a)** Refined
27 map without and **(b)** with a docked atomic model. **(c)** Euler angle distribution showing the particle
28 orientations contributing to final map. **(d)** Surface sampling plot with calculated SCF values. The
29 average SCF from the 3 maps is 0.70.

30

31 **Supplementary Figure 5 | Improvement in resolution for RNAP collected at 0° and 60° tilt**
32 **angles.** RNAP cryo-EM data was collected at two tilt angles (0°, 60°) and equalized for defocus, with
33 72,000 particles used per tilt angle. This figure follows the format of **Fig. 1**. The particles were
34 processed using an identical workflow. **(a)** baseline processing strategy used in Tan et al¹⁵. **(b to h)**
35 Individual steps were added to the workflow and improvements in resolution are plotted as lines.

36

- 1 **Supplementary Movie 1 | Tomographic reconstruction of a tilt-series showing RNAP particles**
- 2 **at the air-water interface.** For colour scheme and description of tilt-series, refer to **Figure 7**.

1 **Supplementary Table 1. Cryo-EM data collection for AAV2**

2

EM data collection / processing							
Tilt Angle (°)	0	10	20	30	40	50	60
Microscope	FEI Titan Krios						
Voltage (kV)	300						
Camera	Gatan K2 Summit						
Mode	Counting						
Energy filter slit width (eV)	No energy filter						
Defocus mean ± std (μm)	1.5±0.3	1.5±0.3	1.5±0.3	1.4±0.4	1.4±0.4	1.5±0.4	1.6±0.4
Exposure time (s)	10						
Number of fractions	200						
Exposure rate (e-/pixel/s)	8.2	8.2	8.2	8.2	8.2	8.2	8.2
Total exposure (e-/Å²)	78.0	78.0	78.0	78.0	78.0	78.0	78.0
Pixel size (Å)	1.026						
Number of micrographs	166	180	194	168	185	181	155
Number of particles (in final map)	7,000						
Symmetry	I						
Resolution (global) (Å)	2.1	2.1	2.1	2.2	2.1	2.1	2.2
Directional Resolution Range (Å)	2.1-2.1	2.1-2.1	2.1-2.1	2.1-2.2	2.1-2.2	2.1-2.1	2.1-2.2
Sphericity of 3DFSC	0.99	0.96	0.99	0.99	0.99	0.99	0.99
SCF Value*	1.00	1.00	1.00	1.00	1.00	1.00	1.00
Map B factor (Å²)	45.9	46.6	47.7	47.3	50.8	50.4	48.7
Map-to-model FSC (global) (Å)	2.1	2.1	2.1	2.1	2.1	2.1	2.2
EMDB ID	EMD-36766	EMD-36767	EMD-36768	EMD-36769	EMD-36770	EMD-36771	EMD-36772

3

4

*The sampling compensation factor (SCF) value is calculated as described (Baldwin and Lyumkis, 2020) and assumes that all orientations have been determined accurately.

5

6

1 **Supplementary Table 2. Cryo-EM data collection statistics for apoferritin (Scripps Research)**

2

EM data collection / processing							
Tilt Angle (°)	0	10	20	30	40	50	60
Microscope	FEI Titan Krios						
Voltage (kV)	300						
Camera	Gatan K3 Quantum						
Mode	Counting (CDS)						
Energy filter slit width (eV)	20						
Defocus mean ± std (μm)	1.4±0.3	1.4±0.4	1.4±0.4	1.3±0.3	1.4±0.4	1.4±0.4	1.5±0.3
Exposure time (s)	1.5						
Number of fractions	100						
Exposure rate (e-/pixel/s)	20.3	20.3	20.3	20.2	20.2	20.3	20.3
Total exposure (e-/Å²)	44.2	44.2	44.1	44.0	44.0	44.1	44.1
Pixel size (Å)	0.830						
Number of micrographs	74	87	79	100	120	91	86
Number of particles (in final map)	17,000						
Symmetry	O						
Resolution (global) (Å)	2.2	2.3	2.3	2.2	2.4	2.3	2.5
Directional Resolution Range (Å)	2.1-2.3	2.2-2.3	2.3-2.4	2.2-2.3	2.3-2.4	2.2-2.3	2.4-2.5
Sphericity of 3DFSC	0.98	0.97	0.99	0.99	0.99	0.99	0.99
SCF Value*	0.91	0.95	0.98	1.00	0.99	1.00	1.00
Map B factor (Å²)	75.2	80.8	86.6	78.2	87.5	86.0	90.1
Map-to-model FSC (global) (Å)	2.2	2.3	2.4	2.3	2.4	2.4	2.5
EMDB ID	EMD-36807	EMD-36809	EMD-36810	EMD-36811	EMD-36812	EMD-36814	EMD-36813

3

4

5 *The sampling compensation factor (SCF) value is calculated as described (Baldwin and Lyumkis, 2020) and assumes that all orientations have been determined accurately.

6

1 **Supplementary Table 3. Cryo-EM data collection statistics for apoferritin (Janelia Research
2 Campus)**
3

EM data collection / processing		
Tilt Angle (°)	0	30
Microscope	FEI Titan Krios	
Voltage (kV)	300	
Camera	Gatan K3 Quantum	
Mode	Counting (CDS)	
Energy filter slit width (eV)	20 eV	
Defocus mean ± std (μm)	0.86 ± 0.53	0.92 ± 0.47
Exposure time (s)	4.1	
Number of fractions	270	
Exposure rate (e-/pixel/s)	7.0	7.0
Total exposure (e-/Å²)	41.2	41.2
Pixel size (Å)	0.83	
Number of micrographs	229	403
Number of particles (in final map)	64,000	
Symmetry	O	
Resolution (global) (Å)	1.93	1.99
Directional Resolution Range (Å)	1.9-2.0	1.9-2.0
Sphericity of 3DFSC	0.99	0.99
SCF Value*	1.00	1.00
Map B factor (Å²)	47.5	50.7
Map-to-model FSC (global) (Å)	1.9	1.9
EMDB ID	EMD-41230	EMD-41231

4
5 *The sampling compensation factor (SCF) value is calculated as described (Baldwin and Lyumkis, 2020) and
6 assumes that all orientations have been determined accurately.
7
8

1 **Supplementary Table 4. Cryo-EM data collection statistics for the 20S Proteasome**

2

EM data collection / processing						
Tilt Angle (°)	0	10	20	30	40	50
Microscope				FEI Titan Krios		
Voltage (kV)				300		
Camera				Gatan K2 Summit		
Mode				Counting		
Energy filter slit width (eV)				No energy filter		
Defocus mean ± std (μm)	2.3±0.4	2.4±0.5	2.3±0.5	2.4±0.5	2.3±0.5	2.3±0.5
Exposure time (s)				14.00		
Number of fractions				70		
Exposure rate (e-/pixel/s)	7.7	7.7	7.7	7.7	7.7	7.7
Total exposure (e-/Å²)	93.8	93.8	93.8	93.8	93.8	93.8
Pixel size (Å)				1.072		
Number of micrographs	82	35	46	108	92	57
Number of particles (in final map)				5,000		
Symmetry				D7		
Resolution (global) (Å)	2.7	2.8	2.8	2.8	2.9	3.0
Directional Resolution Range (Å)	2.6-2.8	2.6-2.8	2.7-2.9	2.7-2.9	2.7-2.9	2.8-3.0
Sphericity of 3DFSC	0.99	0.99	0.99	0.98	0.99	0.97
SCF Value*	0.87	0.89	0.93	0.94	0.96	0.96
Map B factor (Å²)	67.9	70.3	72.9	72.7	73.3	75.1
Map-to-model FSC (global) (Å)	3.2	3.1	3.2	3.2	3.3	3.3

3

4 *The sampling compensation factor (SCF) value is calculated as described (Baldwin and Lyumkis, 2020) and
5 assumes that all orientations have been determined accurately.

6

1 **Supplementary Table 5. Cryo-EM data collection statistics for DPS**

2

EM data collection / processing							
Tilt Angle (°)	0	10	20	30	40	50	60
Microscope	FEI Titan Krios						
Voltage (kV)	300						
Camera	Gatan K3 Quantum						
Mode	Counting (No CDS)						
Energy filter slit width (eV)	20						
Defocus mean ± std (μm)	1.6±0.3	1.5±0.3	1.6±0.3	1.6±0.4	1.6±0.3	1.7±0.4	1.4±0.4
Exposure time (s)	2.54						
Number of fractions	195						
Exposure rate (e-/pixel/s)	16.6	16.6	16.6	16.6	16.6	16.6	16.6
Total exposure (e-/Å²)	59.6	59.6	59.6	59.6	59.6	59.6	59.6
Pixel size (Å)	0.834						
Number of micrographs	15	24	20	35	37	31	32
Number of particles (in final map)	1,750						
Symmetry	T						
Resolution (global) (Å)	2.6	2.8	2.7	3.0	3.2	2.9	3.2
Directional Resolution Range (Å)	2.5-2.8	2.8-3.0	2.6-2.9	2.9-3.3	3.0-3.3	2.8-3.3	3.2-3.5
Sphericity of 3DFSC	0.94	0.98	0.99	0.99	0.98	0.97	0.97
SCF Value*	0.95	0.98	0.99	0.99	0.99	0.99	0.99
Map B factor (Å²)	24.8	35.6	27.2	36.6	34.6	30.0	46.5
Map-to-model FSC (global) (Å)	2.8	3.0	2.9	3.1	3.3	3.4	3.4
EMDB ID	EMD-36816	EMD-36817	EMD-36818	EMD-36819	EMD-36820	EMD-36821	EMD-36822

3

4

5

6

*The sampling compensation factor (SCF) value is calculated as described (Baldwin and Lyumkis, 2020) and assumes that all orientations have been determined accurately.

1 **Supplementary Table 6. Cryo-EM data collection and modeling statistics for RNAP**

2

EM data collection / processing		
Tilt Angle (°)	0	60
Microscope	FEI Titan Krios	
Voltage (kV)	300	
Camera	Gatan K3 Quantum	
Mode	Counting (CDS)	
Energy filter slit width (eV)	20	
Defocus mean ± std (μm)	1.3±0.4	1.8±0.7
Exposure time (s)	0.75	
Number of fractions	50	
Exposure rate (e-/pixel/s)	31.4	35.6
Total exposure (e-/Å ²)	34.2	38.8
Pixel size (Å)	0.830	
Number of micrographs	619	527
Number of particles (in final map)	72,000	
Symmetry	C1	
Resolution (global) (Å)	3.5	3.0
Directional Resolution Range (Å)	3.2-12.3	2.9-5.2
Sphericity of 3DFSC	0.76	0.90
SCF Value*	0.45	0.78
Map B factor (Å ²)	-47.7	-75.9
Map-to-model FSC (global) (Å)	6.8	3.5
EMDB ID	X	X

3

4

5 *The sampling compensation factor (SCF) value is calculated as described (Baldwin and Lyumkis, 2020) and assumes that all orientations have been determined accurately.

1 **Online Methods**

2

3 **Statistics**

4

5 For calculations of Fourier shell correlations (FSC), the FSC cut-off criterion of 0.143^{55} was used.

6

7 **AAV2 production, purification and vitrification**

8

9 AAV2 were produced utilizing the Bac-to-bac system as previously described³⁰. Briefly,
10 recombinant baculoviruses encoding the AAV2 cap gene were used to infect Sf9 insect cells at a
11 multiplicity of infectivity of 5. The infected cells were harvested 72 hours post infection and lysed by
12 three freeze-thaw cycles. Following Benzonase treatment the lysates were clarified and purified using
13 a step iodixanol gradient with subsequent anion exchange chromatography. The sample was dialyzed
14 into 50 mM HEPES, pH 7.4 with 2 mM MgCl₂ and 150 mM NaCl and concentrated with an Apollo 7-
15 ml centrifugal concentrator (Orbital Biosciences, Topsfield, MA).

16

17 To increase particle concentration, double blotting was done⁵⁶. UltrAuFoil R 1.2/1.3 Au 300
18 mesh gold grids (Quantifoil) were used for cryo-EM sample preparation. The grids were plasma
19 treated with the Solarus Plasma Cleaner 950 (Gatan) immediately before sample application to make
20 their surfaces hydrophilic. A $2.5\text{ }\mu\text{L}$ aliquot of AAV2 sample at 2.5 mg mL^{-1} concentration was
21 applied to grids and blotted away using filter paper after 20 s wait time. Another $2.5\text{ }\mu\text{L}$ of the same
22 sample was then re-applied to the grid and blotted after 20 s wait time and then vitrified in liquid
23 ethane using a manual plunger. All operations were performed in a 4 °C cold room at >80%
24 humidity to minimize evaporation and sample degradation.

25

26 **AAV2 cryo-EM data collection and processing**

27

28 Images were recorded on a Titan Krios electron microscope (FEI/Thermo Fisher) equipped with
29 a K2 summit direct detector (Gatan) at 1.026 \AA per pixel in counting mode using the Leginon
30 software package⁵⁷⁻⁶¹. Data collection was performed using a dose of $\sim 78.0\text{ e}^-\text{ \AA}^{-2}$ across 200
31 frames ($50\text{ msec frame}^{-1}$) at a dose rate of $\sim 8.2\text{ e}^-\text{ pix}^{-1}\text{ s}$, using a set nominal defocus range of
32 -0.8 to -2 \mu m with 100 \mu m objective aperture inserted. A total of 1,229 micrographs was recorded
33 over a single 4-day collection using stage shift, across tilt angles of 0° , 10° , 20° , 30° , 40° , 50° and 60°
34 set with stage alpha.

35

1 Movie frames were aligned using MotionCor2⁴¹ with 7 by 7 patches, a grouping of 3 and B-
2 factor of 500 for global alignment and 150 for the patches, initially through Appion⁶², then through
3 RELION^{33,49}. Micrograph CTF estimation was performed using both CTFFind4⁴⁴ for whole
4 micrographs and GCTF³¹ for individual particles within the Appion software package. A subset of
5 eight micrographs was first used for particle picking using Gautomatch (Kai Zhang, unpublished,
6 <https://www.mrc-lmb.cam.ac.uk/kzhang/Gautomatch/>), and particles were extracted and analyzed by
7 2D classification in RELION. 2D class averages that showed clear structural details were used as
8 templates for template-based picking using Gautomatch on all 1,229 micrographs. All particles were
9 then extracted using a box size of 600 pixels and subjected to two initial rounds of 2D classification
10 (binned by 4) to identify and discard false positives such as ice and other obvious contaminants.
11 Following 2D classification, 66,763 particles were re-extracted with the re-centering option in
12 RELION. Finally, the particles from all datasets were again equalized to ensure the distributions of
13 defocus values were consistent across tilts (**Supplementary Table 1**), resulting in 7,000 particles per
14 tilt angle.

15

16 With the equalized dataset of 7,000 particles per tilt angle, cryoSPARC homogeneous refinement
17 was first performed using cryoSPARC *ab initio* map generated from the dataset. Thereafter, cryoSPARC Patch CTF⁴⁸ was performed, followed by RELION CTF refinement⁵⁰, RELION Bayesian
18 polishing⁵⁰, second round of RELION CTF refinement, second round of RELION Bayesian polishing,
19 third round of RELION CTF refinement and finally cryoSPARC Ewald sphere curvature correction⁴⁸.
20 In between these refinements, a cryoSPARC homogeneous refinement was performed in order to
21 obtain the refined map, Euler angles and shifts that would be used for the next refinement. All
22 conversions between RELION and cryoSPARC, were performed using Daniel Asarnow's pyem
23 script⁶³

25

26 For the map-to-model analysis, the PDB-6E9D of the same AAV2 variant was used. The PDB
27 was converted to a map using molmap function in UCSF Chimera⁶⁴. The mask was generated using
28 this PDB initial model which was binarized at 0.01 threshold, extended by 3 pixels, given a soft
29 Gaussian edge of 3 pixels using 'relion_mask_create'. The sharpened AAV2 maps were then
30 compared against the aligned PDB generated maps, using the PDB generated mask, to obtain the
31 map-to-model FSC. EMAN⁶⁵ was used to generate these FSC curves. SCF values were generated
32 using the SCF command line tool^{13,14}, while 3DFSC results were generated using the 3DFSC web
33 server¹⁵. Molecular graphics were generated using UCSF Chimera⁶⁴.

34

35 **Apo ferritin purification and vitrification**

36

1 For data collected at Scripps Research, apoferritin was purchased (Thermo Fisher Scientific) at a
2 concentration of approximately 8 μM (3.5-4.0 mg/mL). Two dilutions were prepared having final
3 concentrations of ~1.6 and 0.8 μM in a buffer containing 50 mM Tris-HCl pH 7.5, 300 mM NaCl 0.5
4 mM TCEP. Untilted, 10° and 20° tilted datasets were collected with grids prepared from ~1.6 μM
5 apoferritin and the rest of the datasets were collected with grids prepared from ~0.8 μM apoferritin.
6

7 UltrAuFoil R 1.2/1.3 Au 300 mesh gold grids (Quantifoil) were used for cryo-EM sample
8 preparation. The grids were plasma treated with the Solarus Plasma Cleaner 950 (Gatan) immediately
9 before sample application to make their surfaces hydrophilic. A 3 μL aliquot of apoferritin sample at
10 ~1.6 or 0.8 μM concentration was applied to grids and then vitrified in liquid ethane using a manual
11 plunger. All operations were performed in a 4 °C cold room at >80% humidity to minimize
12 evaporation and sample degradation.

13
14 For data collected at Janelia Research Campus, apoferritin was purified as described before⁶⁶.
15 Grids were vitrified in a manner similar to the grids prepared for data collection at Scripps Research.
16

17 Apoferritin cryo-EM data collection at Scripps Research and processing

18

19 Images were recorded on a Titan Krios electron microscope (FEI/Thermo Fisher) equipped with
20 a K3 quantum direct detector (Gatan) at 0.830 Å per pixel in counting mode (CDS enabled) using
21 the Leginon software package⁵⁷⁻⁶¹. Energy filter slit width of 20 eV was used. Data collection was
22 performed using a dose of ~44.2 e⁻ Å⁻² across 100 frames (15 msec frame⁻¹) at a dose rate of
23 ~20.3 e⁻ pix⁻¹ s, using a set nominal defocus range of -0.8 to -2 μm with 100 μm objective
24 aperture inserted. A total of 637 micrographs was recorded over a single 4-day collection using stage
25 shift, across tilt angles of 0°, 10°, 20°, 30°, 40°, 50° and 60° set with stage alpha.
26

27 Movie frames were aligned using MotionCor2⁴¹ with 7 by 5 patches, a grouping of 2 and B-
28 factor of 500 for global alignment and 150 for the patches, through RELION^{33,49}. Micrograph CTF
29 estimation was performed using both CTFFind4⁴⁴ for whole micrographs and GCTF³¹ for individual
30 particles within the Appion software package. Template picking using previous apoferritin 2D class
31 averages from routine apoferritin test runs was done. All particles were then extracted using a box
32 size of 320 pixels and subjected to two initial rounds of 2D classification (binned by 4, then by 2) to
33 identify and discard false positives such as ice and other obvious contaminants. Finally, the particles
34 from all datasets were again equalized to ensure the distributions of defocus values were consistent
35 across tilts (**Supplementary Table 2**), resulting in 17,000 particles per tilt angle.
36

1 With the equalized dataset of 17,000 particles per tilt angle, cryoSPARC homogeneous
2 refinement was first performed using cryoSPARC *ab initio* map generated from the dataset.
3 Thereafter, cryoSPARC Patch CTF⁴⁸ was performed, followed by cryoSPARC CTF refinement⁴⁸,
4 RELION Bayesian polishing⁵⁰, second round of cryoSPARC CTF refinement, second round of
5 RELION Bayesian polishing, third round of cryoSPARC CTF refinement and finally cryoSPARC
6 higher order aberration correction⁴⁸. In between these refinements, a cryoSPARC homogeneous
7 refinement was performed in order to obtain the refined map, Euler angles and shifts that would be
8 used for the next refinement. All conversions between RELION and cryoSPARC, were performed
9 using Daniel Asarnow's pyem script⁶³.

10

11 For the map-to-model analysis, the PDB-7A6A of apoferritin was used. The PDB was converted
12 to a map using molmap function in UCSF Chimera⁶⁴. The mask was generated using this PDB initial
13 model which was binarized at 0.01 threshold, extended by 3 pixels, given a soft Gaussian edge of 3
14 pixels using 'relion_mask_create'. The sharpened apoferritin maps were then compared against the
15 aligned PDB generated maps, using the PDB generated mask, to obtain the map-to-model FSC.
16 RELION was used to generate these FSC curves. SCF values were generated using the SCF command
17 line tool^{13,14}, while 3DFSC results were generated using the 3DFSC web server¹⁵. Molecular graphics
18 were generated using UCSF Chimera⁶⁴.

19

20 **Apo ferritin cryo-EM data collection at Janelia Research Campus and processing**

21

22 Images were recorded on a Titan Krios electron microscope (FEI/Thermo Fisher) equipped with
23 a K3 quantum direct detector (Gatan) at 0.830 Å per pixel in counting mode (CDS mode) using the
24 SerialEM⁶⁷. Energy filter slit width of 20 eV was used. Data collection was performed using a dose of
25 ~41.2 e⁻ Å⁻² across 270 frames (15 msec frame⁻¹) at a dose rate of ~7 e⁻ pix⁻¹ s, using an
26 estimated defocus range of -0.2 to -1.7 µm for untilted and -0.1 to -2.8 µm for 30° tilted data
27 collection with 100 µm objective aperture inserted. A total of 637 micrographs was recorded over a
28 single 4-day collection using stage shift, across tilt angles of 0° and 30° set with stage alpha.

29

30 Movie frames were aligned using MotionCor2⁴¹ with 4 by 4 patches, a grouping of 1 and B-
31 factor of 150 for both global alignment and patches through RELION^{33,49}. Micrograph CTF
32 estimation was performed using both cryoSPARC Patch CTF (ref) for whole micrographs within the
33 cryoSPARC GUI and GCTF³¹ for individual particles using a command-line script (ref). Template
34 picking using previous apoferritin 2D class averages from routine apoferritin test runs was done. All
35 particles were then extracted using a box size of 256 pixels and subjected to several rounds of 2D
36 classification to identify and discard false positives such as ice and other obvious contaminants.
37 Finally, the particles from all datasets were again equalized to ensure the distributions of defocus

1 values were consistent across tilts (**Supplementary Table 3**), resulting in 64,000 particles per tilt
2 angle.

3

4 With the equalized dataset of 64,000 particles per tilt angle, cryoSPARC homogeneous
5 refinement was first performed using cryoSPARC *ab initio* map generated from the dataset.
6 Thereafter, cryoSPARC CTF refinement⁴⁸ followed by RELION Bayesian polishing⁵⁰ were
7 performed iteratively for three rounds. In between these refinements, a cryoSPARC homogeneous
8 refinement was performed in order to obtain the refined map, Euler angles and shifts that would be
9 used for the next refinement. All conversions between RELION and cryoSPARC, were performed
10 using Daniel Asarnow's pyem script⁶³.

11

12 For the map-to-model analysis, the PDB-7A6A of apoferritin was used. The PDB was converted
13 to a map using molmap function in UCSF Chimera⁶⁴. The sharpened apoferritin maps were then
14 compared against the aligned PDB generated maps, using the mask generated during final
15 cryoSPARC homogeneous refinement, to obtain the map-to-model FSC. SCF values were generated
16 using the SCF command line tool^{13,14}, while 3DFSC and 2D FSC results were generated using the
17 3DFSC web server¹⁵. Molecular graphics were generated using UCSF Chimera⁶⁴.

18

19 Proteasome vitrification

20

21 Proteasome was obtained as a gift from Yifan Cheng. UltrAuFoil R 1.2/1.3 Au 300 mesh gold
22 grids (Quantifoil) were used for cryo-EM sample preparation. The grids were plasma treated with the
23 Solarus Plasma Cleaner 950 (Gatan, 75% argon/25% oxygen atmosphere at 15 Watts for 30 s)
24 immediately before sample application to make their surfaces hydrophilic. 3 uL of proteasome at 0.3
25 mg mL⁻¹ concentration was applied to grids and plunge-frozen using a Leica EM-grid plunger (Leica
26 Microsystems), with the chamber humidity maintained at 90% humidity and 4°C.

27

28 Proteasome cryo-EM data collection and processing

29

30 Images were recorded on a Titan Krios electron microscope (FEI/Thermo Fisher) equipped with
31 a K2 summit direct detector (Gatan) at 1.07235 Å per pixel in counting mode using the Leginon
32 software package⁵⁷⁻⁶¹. Data collection was performed using a dose of ~93.8 e⁻ Å⁻² across 70 frames
33 (200 msec frame⁻¹) at a dose rate of ~7.7 e⁻ pix⁻¹ s, using a set nominal defocus range of -1.8 to
34 -2.8 μm with 100 μm objective aperture inserted. A total of 420 micrographs was recorded over a
35 single 2-day collection using stage shift, across tilt angles of 0°, 10°, 20°, 30°, 40° and 50° set with
36 stage alpha.

37

1 Movie frames were aligned using MotionCor2⁴¹ with 7 by 7 patches, a grouping of 1 and B-
2 factor of 150 for global alignment and 100 for the patches, through RELION^{33,49}. Micrograph CTF
3 estimation was performed using both CTFFind4⁴⁴ for whole micrographs and GCTF³¹ for individual
4 particles within the Appion software package. Template picking using previous apoferritin 2D class
5 averages from routine proteasome test runs was done. All particles were then extracted using a box
6 size of 400 pixels and subjected to two initial rounds of 2D classification (binned by 4, then by 2) to
7 identify and discard false positives such as ice and other obvious contaminants. Finally, the particles
8 from all datasets were again equalized to ensure the distributions of defocus values were consistent
9 across tilts (**Supplementary Table 4**), resulting in 5,000 particles per tilt angle.
10

11 With the equalized dataset of 5,000 particles per tilt angle, cryoSPARC homogeneous refinement
12 was first performed using cryoSPARC *ab initio* map generated from the dataset. Thereafter,
13 cryoSPARC Patch CTF⁴⁸ was performed, followed by cryoSPARC CTF refinement⁴⁸, RELION
14 Bayesian polishing⁵⁰ and final round of cryoSPARC CTF refinement. In between these refinements, a
15 cryoSPARC homogeneous refinement was performed to obtain the refined map, Euler angles and
16 shifts that would be used for the next refinement. All conversions between RELION and cryoSPARC,
17 were performed using Daniel Asarnow's pyem script⁶³.
18

19 For the map-to-model analysis, the PDB-1YAR of apoferritin was used. The PDB was converted
20 to a map using molmap function in UCSF Chimera⁶⁴. The mask was generated using this PDB initial
21 model which was binarized at 0.01 threshold, extended by 3 pixels, given a soft Gaussian edge of 3
22 pixels using 'relion_mask_create'. The sharpened proteasome maps were then compared against the
23 aligned PDB generated maps, using the PDB generated mask, to obtain the map-to-model FSC.
24 RELION was used to generate these FSC curves. SCF values were generated using the SCF command
25 line tool^{13,14}, while 3DFSC results were generated using the 3DFSC web server¹⁵. Molecular graphics
26 were generated using UCSF Chimera⁶⁴.
27

28 DPS purification and vitrification

30 A modified pET15b expression plasmid for Escherichia coli DPS, which yields the target protein
31 fused to an N-terminal hexahistidine tag and TEV-protease cleavage site, was provided by
32 Christopher Russo (MRC-LMB). DPS protein was heterologously over-expressed in the E. coli
33 BL21(DE3)-RIPL (Agilent) expression host. E. coli cultures were grown at 37 °C in TB medium
34 (supplemented with 50 µg/ml ampicillin) to an optical density (600 nm) of 1.5, induced with 0.5 mM
35 isopropyl-β-D-thiogalactoside, and allowed to grow for an additional 16 h at 18°C. Bacterial cells
36 were harvested by centrifugation, resuspended in lysis buffer (50 mM Tris-HCl, pH 8.0; 0.5 M NaCl;
37 20 mM imidazole; 1% v/v Tween20; 10% v/v glycerol; and 10 mM 2-mercaptoethanol), and lysed by

1 sonication. The DPS protein was isolated from the lysate by affinity chromatography with nickel
2 nitrilotriacetic-acid-coupled agarose (Thermo Scientific), and eluted with lysis buffer containing 0.25
3 M imidazole. The partially purified DPS protein (His₆-tag uncleaved) was then further purified by
4 gel-filtration chromatography on a Superdex 200 HR26/60 column (Amersham Biosciences), with a
5 column buffer containing 50 mM Tris-HCl, pH 8.0, 0.5 M NaCl, and 10 mM 2-mercaptoethanol. The
6 final purified DPS protein was dialyzed into a buffer containing 12.5 mM Tris-HCl, pH 8.0, 0.05 M
7 NaCl, and 10 mM 2-mercaptoethanol, and then concentrated to ~10mg/ml. For estimation of the size
8 of the DPS oligomer by size-exclusion chromatography, the elution volume of DPS was compared to
9 that of a panel of other proteins with a similar or smaller oligomer size.
10

11 UltrAuFoil R 1.2/1.3 Au 300 mesh gold grids (Quantifoil) were used for cryo-EM sample
12 preparation. The grids were plasma treated with the Solarus Plasma Cleaner 950 (Gatan) immediately
13 before sample application to make their surfaces hydrophilic. A 2.5 μ L aliquot of DPS sample at
14 0.0625 mg mL⁻¹ concentration was applied to grids and then vitrified in liquid ethane using a
15 manual plunger. All operations were performed in a 4 °C cold room at >80% humidity to minimize
16 evaporation and sample degradation.
17

18 DPS cryo-EM data collection and processing

19

20 Images were recorded on a Titan Krios electron microscope (FEI/Thermo Fisher) equipped with
21 a K3 quantum direct detector (Gatan) at 0.834 Å per pixel in counting mode (CDS enabled) using
22 the Leginon software package⁵⁷⁻⁶¹. Energy filter slit width of 20 eV was used. Data collection was
23 performed using a dose of ~59.6 e⁻ Å⁻² across 195 frames (13 msec frame⁻¹) at a dose rate of
24 ~16.6 e⁻ pix⁻¹ s, using a set nominal defocus range of -1.2 to -2.0 μm with 100 μm objective
25 aperture inserted. A total of 194 micrographs was recorded over a single 2-day collection using stage
26 shift, across tilt angles of 0°, 10°, 20°, 30°, 40°, 50° and 60° set with stage alpha.
27

28 Movie frames were aligned using MotionCor2⁴¹ with 7 by 5 patches, a grouping of 1 and B-
29 factor of 500 for global alignment and 150 for the patches, through RELION^{33,49}. Micrograph CTF
30 estimation was performed using both CTFFind4⁴⁴ for whole micrographs and GCTF³¹ for individual
31 particles within the Appion software package. CryoSPARC blob picker was used to pick particles
32 from all micrographs, and an initial 2D classification was done to generate templates for template
33 picking. All template picked particles were then extracted using a box size of 256 pixels and subjected
34 to two initial rounds of 2D classification (binned by 4, then by 2) to identify and discard false
35 positives such as ice and other obvious contaminants. Finally, the particles from all datasets were
36 again equalized to ensure the distributions of defocus values were consistent across tilts
37 (**Supplementary Table 5**), resulting in 1,750 particles per tilt angle.

1

2 With the equalized dataset of 1,750 particles per tilt angle, cryoSPARC homogeneous refinement
3 was first performed using cryoSPARC *ab initio* map generated from the dataset. Thereafter,
4 cryoSPARC Patch CTF⁴⁸ was performed, followed by RELION Bayesian polishing⁵⁰, second round
5 of RELION Bayesian polishing⁵⁰, cryoSPARC CTF refinement⁴⁸, and finally higher order aberration
6 correction using RELION⁵⁰. In between these refinements, a cryoSPARC homogeneous refinement
7 was performed to obtain the refined map, Euler angles and shifts that would be used for the next
8 refinement. All conversions between RELION and cryoSPARC, were performed using Daniel
9 Asarnow's pyem script⁶³.

10

11 For the map-to-model analysis, the PDB- 6GCM of DPS was used. The PDB was converted to a
12 map using molmap function in UCSF Chimera⁶⁴. The mask was generated using this PDB initial
13 model which was binarized at 0.01 threshold, extended by 3 pixels, given a soft Gaussian edge of 3
14 pixels using 'relion_mask_create'. The sharpened proteasome maps were then compared against the
15 aligned PDB generated maps, using the PDB generated mask, to obtain the map-to-model FSC.
16 RELION was used to generate these FSC curves. SCF values were generated using the SCF command
17 line tool^{13,14}, while 3DFSC results were generated using the 3DFSC web server¹⁵. Molecular graphics
18 were generated using UCSF Chimera⁶⁴.

19

20 **RNAP purification and vitrification**

21

22 The expression plasmids for *E. coli* RNA polymerase (deposited by Seth Darst lab) was
23 purchased from Addgene. We followed previous purification methods⁶⁸ with modification.
24 pEcRNAP6 (Addgene # 128940) and pACYCDuet-LEc-rpoZ (Addgene # 128837) were co-
25 transformed to BL21 (DE3) competent cells. 0.25 mM of IPTG was added to cell culture when O.D.
26 reached 0.6 and protein were expressed in 20 °C for overnight. Cells were collected and resuspended
27 in Buffer A [50 mM Tris (pH 7.4), 500 mM NaCl, 5% (v/v) glycerol, 2 mM β-mercaptoethanol (BME)
28 and 1X EDTA-free protease inhibitor (Sigma-Aldrich)]. After lysis and centrifugation, cell lysate was
29 loaded to Ni-NTA resin and washed with Buffer A + 20 mM imidazole, Buffer A (300 mM NaCl) +
30 30 mM imidazole and eluted by Buffer A (300 mM NaCl) + 250 mM imidazole. Eluted sample was
31 diluted with Buffer A (no salt) 2 times to reduce NaCl concentration to 150 mM. After dilution,
32 sample was loaded onto HiTrap Heparin column, and purified by increasing NaCl concentration from
33 150 mM to 800 mM. For anion exchange purification, heparin elute was dialyzed against Buffer B
34 (20 mM HEPES pH 8.0, 100 mM NaCl, 5% (v/v) glycerol, 1 mM DTT). After dialysis, the sample
35 was loaded into HiTrap Q column. *E. coli* RNA polymerase ($\alpha_2\beta'\beta\omega$) was purified by increasing

1 NaCl concentration from 100 mM to 800 mM. During concentration, buffer was changed to Buffer B
2 with 150 mM NaCl, flash frozen in liquid nitrogen and stored in -80 °C for further use.
3

4 For vitrification, mini-scaffold containing RNA, tsDNA and ntsDNA with molar ratio of
5 1.2:1:1.2 were annealed in 1X EB. To form the elongation complex, purified *E. coli* RNAP were
6 mixed with prepared Mini-scaffold with molar ratio 1:1.3 and incubated in ice for 1 hour. Final 4 mM
7 of MgCl₂ in 1X EB were added to elongation complex and incubated in ice for 30 min. The final *E.*
8 *coli* RNAP concentration was 15~18 mg/ml. If dilution was needed, 4 mM substrate nucleotide
9 triphosphate and 4 mM MgCl₂ in 1X EB were used.
10

11 Grids were prepared using a homemade manual plunging apparatus in a cold room where the
12 temperature was between 3-5°C and humidity was in excess of 85%. A range of 0.05-0.4 mg/ml of
13 sample concentration was used to prepare grids of different concentration, and UltrAufoil R1.2/1.3
14 (Quantifoil) grids were used for all conditions.
15

16 **RNAP cryo-EM data collection and processing**

17

18 In order to initially gauge the number of micrographs/particles that would be needed to exceed
19 ~4 Å resolution, on-the-fly data processing using cryoSPARC Live was performed. For untilted
20 specimen stage tilt, a concentration of 0.4 mg/ml of RNAP on R1.2/1.3 UltrAufoil grids was used.
21 This allowed for a monodisperse distribution of particles with uniform ice thickness and with most
22 squares in the grid that were of imageable quality when viewed at low magnification. We found that
23 grids prepared with 0.1-0.2 mg/ml gave a good distribution of non-overlapping particles and
24 proceeded to collect data with these grids for the 60° dataset. The behavior of particles at lower
25 concentrations was different than the concentration of 0.4 mg/ml that was used for untilted data
26 collection. Many squares were not imageable due to empty holes with no vitreous ice. Carefully
27 selecting imageable areas over two grids enabled collection of a comparable amount of particles to
28 that of untilted data collection scheme. For the 51° dataset, a grid prepared with 0.3 mg/ml of RNAP
29 was used, which was less than what was used for untilted data collection but more than what was used
30 for 60° tilted collection. At this concentration, many squares were imageable, although we observed a
31 more pronounced effect of squares having empty holes compared to the grid used for untilted data
32 collection.
33

34 For the untilted dataset, a total of 638 micrographs was collected. After selecting micrographs
35 with a CTF fit limit of under 6 Å, 619 micrographs were left with approximately 280
36 particles/micrograph. With this strategy, a sub-4 Å map was obtained using the standard data
37 processing pipeline of cryoSPARC Live^{32,48}. For the 60° dataset, a total of 826 micrographs was

1 collected. After selecting micrographs with a CTF fit limit of under 6 Å, 527 micrographs were left
2 with approximately 137 particles/micrograph. For the 51° dataset, a total of 1232 micrographs were
3 collected. After selecting micrographs with a CTF fit limit of under 6 Å, 1024 micrographs were left
4 with approximately 786 particles/micrograph.

5

6 Movies were initially aligned using UCSF MotionCor2⁴¹ using 5 by 5 patches. Initial CTF
7 estimates were derived using patch-based CTF estimation in cryoSPARC⁴⁸. Particles were picked
8 using blob picker in cryoSPARC, followed by one round of 2D classification. Particle class averages
9 with high resolution features were used as templates for template-based particle picking in
10 cryoSPARC. Particles were extracted from the micrographs and subjected to iterative 2D
11 classification to obtain a clean stack of particles. GCTF³¹ was then applied to obtain per-particle
12 defocus values, which we found in our previous report yielded the highest-resolution reconstructions
13 of specimens collected with the stage tilted¹⁵, in comparison to CTFFind3⁴⁷ and CTFTilt⁴⁷. An equal
14 number of particles were then extracted from 0° and 60° tilt angle, in a manner that ensures that the
15 spread of defocus values is similar across the different datasets (**Supplementary Table 6**), resulting
16 in 72,000 particles per tilt angle.

17

18 Thereafter, 3D reconstructions were derived using cryoSPARC homogenous refinement⁴⁸,
19 cryoSPARC CTF refinement⁴⁸ and RELION Bayesian polishing⁵⁰ until no further improvements in
20 global resolution were observed. For processing in RELION, particle metadata STAR files were
21 generated from cryoSPARC homogeneous refinement metadata files using pyem module and
22 cspars2star.py script⁶³.

23

24 For 51° tilted dataset, similar data-processing steps were employed, except three 3D classes were
25 obtained from one round of heterogeneous refinement from a clean stack of particles. Euler angles
26 from these 3 classes were used for computing SCF¹³ and the mean of 3 SCF values was reported.

27

28 For the map-to-model analysis, a refined atomic map of RNAP was used (unpublished). The
29 PDB was converted to a map using molmap function in UCSF Chimera⁶⁴. The mask was generated
30 using this PDB initial model which was binarized at 0.01 threshold, extended by 3 pixels, given a soft
31 Gaussian edge of 3 pixels using ‘relion_mask_create’. The sharpened proteasome maps were then
32 compared against the aligned PDB generated maps, using the PDB generated mask, to obtain the
33 map-to-model FSC. RELION was used to generate these FSC curves. SCF values were generated
34 using the SCF command line tool^{13,14}, while 3DFSC results were generated using the 3DFSC web
35 server¹⁵. Molecular graphics were generated using UCSF Chimera⁶⁴.

36

37 Cryo-electron tomography data acquisition

1

2 Tomograms were collected for an RNA polymerase (0.3 mg/ml) grid using a Thermo Fisher
3 Titan Krios TEM operating at 300 keV at the Pacific Northwest Center for Cryo-EM (PNCC). Gatan
4 K3 Summit direct electron detector equipped with an energy filter operated in zero-loss mode (with
5 the slit width of 20 eV) was used. The tomography data were acquired from specific regions of the
6 grid that were not previously exposed and were similar in vitrification quality to the squares used for
7 single-particle data collection. The SerialEM software⁶⁷ was utilized for data collection, employing a
8 dose-symmetric scheme starting at 0° and capturing alternating negative and positive tilts in 3°
9 increments. The tilt angles for the tomograms ranged from -48° to +54°, while the nominal defocus
10 range during tilt series collection was -2 to -4 μm. Each tilt was recorded as movie frames with 10
11 sub-frames in counting mode, utilizing a per-frame dose of approximately 0.23 e/Å². The
12 magnification was set to 42Kx, resulting in a pixel size of 1.06 Å/pixel. A total of 25 tomograms were
13 collected for the RNA polymerase sample, and among them, 5 with best alignment statistics were
14 subjected to further processing and data analysis.

15

16 **Cryo-electron tomography data processing**

17

18 Image stacks were subjected to frame-alignment and CTF estimation in Warp⁶⁹. The frame-
19 aligned averages were then exported to IMOD⁷⁰ for further processing. The Etomo module in IMOD
20 was utilized for tomogram alignment using patch tracking and subsequent tomogram reconstruction.
21 Prior to reconstruction, the aligned stack was binned by a factor of six (resulting in a pixel size of 6.36
22 Å) and a standard Gaussian filter was applied. Particles within the tomogram exhibited a tilt
23 perpendicular to the field of view, approximately 4° away from the X-axis. For further validation, we
24 extracted 25 micrographs at 0° tilt and performed CTF and tilt angle estimation in cryoSPARC using
25 the Manually Curate Exposures function based on the defocus gradient⁴⁸. The observed tilt in the
26 tomograms can be attributed either to a residual tilt angles present on the microscope stage or to a
27 deformation of the grid caused during vitrification. To address this residual tilt, the coarse alignment
28 and reconstruction were then recalculated by applying a -4° tilt to the x-axis. Tomograms were
29 visualized in IMOD using the "3dmod Slicer" view.

30

31 Ice-thickness measurement was performed by employing a previously described method based
32 on template matching and particle picking⁷¹. The positions of the top-most and bottom-most particles
33 at the air-water interface were then used to delineate the ice boundary. To generate the reference
34 model and mask required for template matching, the final RNA polymerase map obtained from the 60°
35 tilted single particle analysis data collection. This map was low-pass filtered to 20 Å, resized, and
36 resampled to match the pixel size of the tomogram (6.36 Å pixel size and a voxel size of 48). The
37 contrast of the map was inverted to serve as the reference model. The same map was used to create

1 the soft-edge mask. The processing steps, including low-pass filtering, contrast inversion, map down-
2 sampling, and mask generation, were carried out using the e2proc3d.py script in EMAN2⁷².

3

4 For particle picking, an additional mask was generated in the Amira software (Thermo Fisher
5 Scientific) to exclude the gold edges of the grid in order to avoid false positives during template
6 matching. Template matching and particle picking were performed using PyTom⁷³. The resulting
7 particle positions and initial orientations were then converted to the RELION 3.1 STAR file format⁴⁹.
8 To visualize the position of each particle within the tomogram, the ArtiaX⁷⁴ plugin in ChimeraX⁷⁵
9 was utilized (**Figure 7 and Supplementary Movie 1**). The ice-thickness measurement was conducted
10 using ChimeraX by determining the distance between the particles located at the air-water interface.

11

12 Calculation of SCF values for predicting optimal stage tilt angles

13

14 The construction of **Fig 10** involves the evaluation of the sampling compensation factor (SCF*)
15 introduced in Baldwin and Lyumkis^{13,14}. All of the distributions represented in Fig 9 are shown in
16 detail in this previous work. To obtain the values of the SCF, the graphical user interface (GUI)
17 described in Baldwin and Lyumkis¹⁴ was used after loading the 3 column files representing the Euler
18 angles for 10000 projections of the described distribution. A color map was chosen to effectively
19 demonstrate the transition region from good to poor distributions. We take this transition value of the
20 SCF to be 0.81, which is the theoretical and empirical value of the SCF for pure side views and
21 describes a fully sampled reconstruction. A set of side view projections fill the entirety of Fourier
22 space, but show some variation in SNR, with accentuated SNR along the symmetry axis and lower
23 values away from this axis.

24

25

1 **Accession codes and deposition**

2 All raw movie frames, micrographs, the particle stack, and relevant metadata files for the AAV2,
3 Apoferritin, DPS, and RNAP untilted and tilted datasets are deposited in the EMPIAR database as
4 EMPIAR-XXXX. The electron potential maps of AAV2 at various tilts are deposited into the electron
5 microscopy databank as EMD-36766 (0°), EMD-36767 (10°), EMD-36768 (20°), EMD-36769 (30°),
6 EMD-36770 (40°), EMD-36771 (50°) and EMD-36772 (60°). The electron potential maps of
7 apoferritin (Scripps Research) at various tilts are deposited into the electron microscopy databank as
8 EMD-36807 (0°), EMD-36809 (10°), EMD-36810 (20°), EMD-36811 (30°), EMD-36812 (40°),
9 EMD-36814 (50°) and EMD-36813 (60°). The electron potential maps of apoferritin (Janelia
10 Research Campus) at various tilts are deposited into the electron microscopy databank as EMD-41230
11 (0°) and EMD-41231 (30°). The electron potential maps of DPS at various tilts are deposited into the
12 electron microscopy databank as EMD-36816 (0°), EMD-36817 (10°), EMD-36818 (20°), EMD-
13 36819 (30°), EMD-36820 (40°), EMD-36821 (50°) and EMD-36822 (60°). The model for RNAP has
14 been deposited into the PDB as PDB-XXXX. Other data are available from the corresponding authors
15 upon request.

16

1 **Online Methods References**

- 2 1 Lyumkis, D. Challenges and opportunities in cryo-EM single-particle analysis. *Journal of
3 Biological Chemistry* **294**, 5181-5197 (2019).
- 4 2 Chua, E. Y. *et al.* Better, Faster, Cheaper: Recent Advances in Cryo-Electron Microscopy.
5 *Annual Review of Biochemistry* **91** (2022).
- 6 3 Tan, Y. Z. & Carragher, B. Seeing Atoms: Single-Particle Cryo-EM Breaks the Atomic Barrier.
7 *Molecular Cell* **80**, 938-939 (2020).
- 8 4 Nakane, T. *et al.* Single-particle cryo-EM at atomic resolution. *Nature* **587**, 152-156 (2020).
- 9 5 Yip, K. M., Fischer, N., Paknia, E., Chari, A. & Stark, H. Atomic-resolution protein structure
10 determination by cryo-EM. *Nature* **587**, 157-161 (2020).
- 11 6 Zhang, K., Pintilie, G. D., Li, S., Schmid, M. F. & Chiu, W. Resolving individual atoms of protein
12 complex by cryo-electron microscopy. *Cell research* **30**, 1136-1139 (2020).
- 13 7 Wu, M. & Lander, G. C. Present and emerging methodologies in cryo-EM single-particle
14 analysis. *Biophysical Journal* **119**, 1281-1289 (2020).
- 15 8 Grigorieff, N. Frealign: an exploratory tool for single-particle cryo-EM. *Methods in
16 enzymology* **579**, 191-226 (2016).
- 17 9 Penczek, P., Radermacher, M. & Frank, J. Three-dimensional reconstruction of single
18 particles embedded in ice. *Ultramicroscopy* **40**, 33-53 (1992).
- 19 10 Carragher, B. *et al.* Current outcomes when optimizing 'standard' sample preparation for
20 single-particle cryo-EM. *Journal of microscopy* **276**, 39-45 (2019).
- 21 11 Glaeser, R. M. Preparing Better Samples for Cryo-Electron Microscopy: Biochemical
22 Challenges Do not End with Isolation and Purification. *Annual Review of Biochemistry* **90**
23 (2021).
- 24 12 Vilas, J. L., Tagare, H. D., Vargas, J., Carazo, J. M. & Sorzano, C. O. S. Measuring local-
25 directional resolution and local anisotropy in cryo-EM maps. *Nature communications* **11**, 1-7
26 (2020).
- 27 13 Baldwin, P. R. & Lyumkis, D. Non-uniformity of projection distributions attenuates resolution
28 in Cryo-EM. *Progress in biophysics and molecular biology* **150**, 160-183 (2020).
- 29 14 Baldwin, P. R. & Lyumkis, D. Tools for visualizing and analyzing Fourier space sampling in
30 Cryo-EM. *Progress in Biophysics and Molecular Biology* **160**, 53-65 (2021).
- 31 15 Tan, Y. Z. *et al.* Addressing preferred specimen orientation in single-particle cryo-EM through
32 tilting. *Nature methods* **14**, 793-796 (2017).
- 33 16 Diebolder, C. A., Faas, F. G., Koster, A. J. & Koning, R. I. Conical Fourier shell correlation
34 applied to electron tomograms. *Journal of structural biology* **190**, 215-223 (2015).
- 35 17 Dudkina, N. V., Kudryashev, M., Stahlberg, H. & Boekema, E. J. Interaction of complexes I, III,
36 and IV within the bovine respirasome by single particle cryoelectron tomography.
37 *Proceedings of the National Academy of Sciences* **108**, 15196-15200 (2011).
- 38 18 Lyumkis, D. in *Single-particle cryo-electron microscopy (cryo-EM): Progress, challenges, and
39 perspectives for further improvement*
40 4-45 - 44-59 (2021).
- 41 19 Herzik, M. A., Wu, M. & Lander, G. C. High-resolution structure determination of sub-100
42 kDa complexes using conventional cryo-EM. *Nature communications* **10**, 1-9 (2019).
- 43 20 Huang, G. *et al.* Structure of the cytoplasmic ring of the Xenopus laevis nuclear pore complex
44 by cryo-electron microscopy single particle analysis. *Cell research* **30**, 520-531 (2020).
- 45 21 Zhang, Y. *et al.* Molecular architecture of the luminal ring of the Xenopus laevis nuclear pore
46 complex. *Cell research* **30**, 532-540 (2020).
- 47 22 Wright, E. R., Iancu, C. V., Tivol, W. F. & Jensen, G. J. Observations on the behavior of
48 vitreous ice at~ 82 and~ 12 K. *Journal of structural biology* **153**, 241-252 (2006).
- 49 23 Glaeser, R. M. *et al.* Factors that influence the formation and stability of thin, cryo-EM
50 specimens. *Biophysical Journal* **110**, 749-755 (2016).

- 1 24 Zheng, L. *et al.* Uniform thin ice on ultraflat graphene for high-resolution cryo-EM. *Nature Methods*, 1-8 (2022).
- 2 25 Rice, W. J. *et al.* Routine determination of ice thickness for cryo-EM grids. *Journal of structural biology* **204**, 38-44 (2018).
- 3 26 Brilot, A. F. *et al.* Beam-induced motion of vitrified specimen on holey carbon film. *Journal of structural biology* **177**, 630-637 (2012).
- 4 27 Campbell, M. G. *et al.* Movies of ice-embedded particles enhance resolution in electron cryo-microscopy. *Structure* **20**, 1823-1828 (2012).
- 5 28 Li, X. *et al.* Electron counting and beam-induced motion correction enable near-atomic-resolution single-particle cryo-EM. *Nature methods* **10**, 584-590 (2013).
- 6 29 Thorne, R. E. Hypothesis for a mechanism of beam-induced motion in cryo-electron microscopy. *IUCrJ* **7**, 416-421 (2020).
- 7 30 Tan, Y. Z. *et al.* Sub-2 Å Ewald curvature corrected structure of an AAV2 capsid variant. *Nature communications* **9**, 1-11 (2018).
- 8 31 Zhang, K. Gctf: Real-time CTF determination and correction. *Journal of structural biology* **193**, 1-12 (2016).
- 9 32 Punjani, A., Rubinstein, J. L., Fleet, D. J. & Brubaker, M. A. cryoSPARC: algorithms for rapid unsupervised cryo-EM structure determination. *Nature methods* **14**, 290-296 (2017).
- 10 33 Scheres, S. H. Beam-induced motion correction for sub-megadalton cryo-EM particles. *elife* **3**, e03665 (2014).
- 11 34 Zivanov, J., Nakane, T. & Scheres, S. H. A Bayesian approach to beam-induced motion correction in cryo-EM single-particle analysis. *IUCrJ* **6**, 5-17 (2019).
- 12 35 Russo, C. J. & Passmore, L. A. Ultrastable gold substrates for electron cryomicroscopy. *Science* **346**, 1377-1380 (2014).
- 13 36 Naydenova, K. *et al.* CryoEM at 100 keV: a demonstration and prospects. *IUCrJ* **6**, 1086-1098 (2019).
- 14 37 Chen, J., Noble, A. J., Kang, J. Y. & Darst, S. A. Eliminating effects of particle adsorption to the air/water interface in single-particle cryo-electron microscopy: Bacterial RNA polymerase and CHAPSO. *Journal of structural biology: X* **1**, 100005 (2019).
- 15 38 Chen, J. *et al.* Stepwise promoter melting by bacterial RNA polymerase. *Molecular cell* **78**, 275-288. e276 (2020).
- 16 39 Neselu, K. *et al.* Measuring the effects of ice thickness on resolution in single particle cryo-EM. *Journal of Structural Biology: X*, 100085 (2023).
- 17 40 Martynowycz, M. W., Clabbers, M. T., Unge, J., Hattne, J. & Gonen, T. Benchmarking the ideal sample thickness in cryo-EM. *Proceedings of the National Academy of Sciences* **118**, e2108884118 (2021).
- 18 41 Zheng, S. Q. *et al.* MotionCor2: anisotropic correction of beam-induced motion for improved cryo-electron microscopy. *Nature methods* **14**, 331-332 (2017).
- 19 42 Rubinstein, J. L. & Brubaker, M. A. Alignment of cryo-EM movies of individual particles by optimization of image translations. *Journal of structural biology* **192**, 188-195 (2015).
- 20 43 Grant, T. & Grigorieff, N. Measuring the optimal exposure for single particle cryo-EM using a 2.6 Å reconstruction of rotavirus VP6. *elife* **4**, e06980 (2015).
- 21 44 Rohou, A. & Grigorieff, N. CTFFIND4: Fast and accurate defocus estimation from electron micrographs. *Journal of structural biology* **192**, 216-221 (2015).
- 22 45 Stagg, S. M., Noble, A. J., Spilman, M. & Chapman, M. S. ResLog plots as an empirical metric of the quality of cryo-EM reconstructions. *Journal of structural biology* **185**, 418-426 (2014).
- 23 46 Su, M. goCTF: Geometrically optimized CTF determination for single-particle cryo-EM. *Journal of structural biology* **205**, 22-29 (2019).
- 24 47 Mindell, J. A. & Grigorieff, N. Accurate determination of local defocus and specimen tilt in electron microscopy. *Journal of structural biology* **142**, 334-347 (2003).

- 1 48 Punjani, A. Algorithmic advances in single particle cryo-EM data processing using CryoSPARC.
2 49 *Microscopy and Microanalysis* **26**, 2322-2323 (2020).
- 3 49 Zivanov, J. et al. New tools for automated high-resolution cryo-EM structure determination
4 50 in RELION-3. *elife* **7**, e42166 (2018).
- 5 50 Zivanov, J., Nakane, T. & Scheres, S. H. Estimation of high-order aberrations and anisotropic
6 51 magnification from cryo-EM data sets in RELION-3.1. *IUCrJ* **7**, 253-267 (2020).
- 7 51 Herzik Jr, M. A., Wu, M. & Lander, G. C. High-resolution structure determination of sub-100
8 52 kDa complexes using conventional cryo-EM. *Nature communications* **10**, 1032 (2019).
- 9 52 Palovcak, E., Asarnow, D., Campbell, M. G., Yu, Z. & Cheng, Y. Enhancing the signal-to-noise
10 53 ratio and generating contrast for cryo-EM images with convolutional neural networks. *IUCrJ*
11 53 **7**, 1142-1150 (2020).
- 12 53 Bepler, T., Kelley, K., Noble, A. J. & Berger, B. Topaz-Denoise: general deep denoising models
13 54 for cryoEM and cryoET. *Nature communications* **11**, 5208 (2020).
- 14 54 Naydenova, K., Jia, P. & Russo, C. J. Cryo-EM with sub-1 Å specimen movement. *Science* **370**,
15 55 223-226 (2020).
- 16 55 Rosenthal, P. B. & Henderson, R. Optimal determination of particle orientation, absolute
17 56 hand, and contrast loss in single-particle electron cryomicroscopy. *J Mol Biol* **333**, 721-745
18 56 (2003).
- 19 56 Snijder, J. et al. Vitrification after multiple rounds of sample application and blotting
20 57 improves particle density on cryo-electron microscopy grids. *Journal of structural biology*
21 57 **198**, 38-42 (2017).
- 22 57 Suloway, C. et al. Automated molecular microscopy: the new Leginon system. *Journal of
23 58 structural biology* **151**, 41-60 (2005).
- 24 58 Carragher, B. et al. Leginon: an automated system for acquisition of images from vitreous ice
25 59 specimens. *Journal of structural biology* **132**, 33-45 (2000).
- 26 59 Cheng, A. et al. Leginon: New features and applications. *Protein Science* **30**, 136-150 (2021).
- 27 60 Potter, C. S. et al. Leginon: a system for fully automated acquisition of 1000 electron
28 61 micrographs a day. *Ultramicroscopy* **77**, 153-161 (1999).
- 29 61 Aiyyer, S., Strutzenberg, T. S., Bowman, M. E., Noel, J. P. & Lyumkis, D. Single-Particle Cryo-
30 62 EM Data Collection with Stage Tilt using Leginon. *JoVE (Journal of Visualized Experiments)*,
31 62 e64136 (2022).
- 32 62 Lander, G. C. et al. Appion: an integrated, database-driven pipeline to facilitate EM image
33 63 processing. *Journal of structural biology* **166**, 95-102 (2009).
- 34 63 Asarnow, D., Palovcak, E. & Cheng, Y. UCSF pyem v0. 5. Zenodo. Ausio, J., Borochov, N.,
35 64 Seger, D., and Eisenberg, H.(1984). *Interaction of chromatin with NaCl and MgCl₂. Solubility
36 64 and binding studies, transition to and characterization of the higher-order structure*. *J. Mol.
37 64 Biol* **177**, 373-398 (2019).
- 38 64 Pettersen, E. F. et al. UCSF Chimera—a visualization system for exploratory research and
39 65 analysis. *J Comput Chem* **25**, 1605-1612 (2004).
- 40 65 Ludtke, S. J., Baldwin, P. R. & Chiu, W. EMAN: semiautomated software for high-resolution
41 66 single-particle reconstructions. *Journal of structural biology* **128**, 82-97 (1999).
- 42 66 Zou, W. et al. Expression, purification, and characterization of recombinant human H-chain
43 67 ferritin. *Prep Biochem Biotechnol* **46**, 833-837 (2016).
44 67 <https://doi.org/10.1080/10826068.2016.1141300>
- 45 67 Mastronarde, D. N. Automated electron microscope tomography using robust prediction of
46 68 specimen movements. *Journal of structural biology* **152**, 36-51 (2005).
- 47 68 Twist, K. A. et al. A novel method for the production of in vivo-assembled, recombinant
48 69 Escherichia coli RNA polymerase lacking the α C-terminal domain. *Protein Science* **20**, 986-
49 69 995 (2011).
- 50 69 Tegunov, D. & Cramer, P. Real-time cryo-electron microscopy data preprocessing with Warp.
51 69 *Nature methods* **16**, 1146-1152 (2019).

- 1 70 Kremer, J. R., Mastronarde, D. N. & McIntosh, J. R. Computer visualization of three-dimensional image data using IMOD. *Journal of structural biology* **116**, 71-76 (1996).
- 2
- 3 71 Noble, A. J. *et al.* Routine single particle CryoEM sample and grid characterization by tomography. *Elife* **7**, e34257 (2018).
- 4
- 5 72 Tang, G. *et al.* EMAN2: an extensible image processing suite for electron microscopy. *Journal of structural biology* **157**, 38-46 (2007).
- 6
- 7 73 Hrabe, T. Localize. pytom: a modern webserver for cryo-electron tomography. *Nucleic acids research* **43**, W231-W236 (2015).
- 8
- 9 74 Ermel, U. H., Arghittu, S. M. & Frangakis, A. S. ArtiaX: An electron tomography toolbox for the interactive handling of sub-tomograms in UCSF ChimeraX. *Protein science* **31**, e4472 (2022).
- 10
- 11
- 12 75 Pettersen, E. F. *et al.* UCSF ChimeraX: Structure visualization for researchers, educators, and developers. *Protein Science* **30**, 70-82 (2021).
- 13
- 14

Figure 1

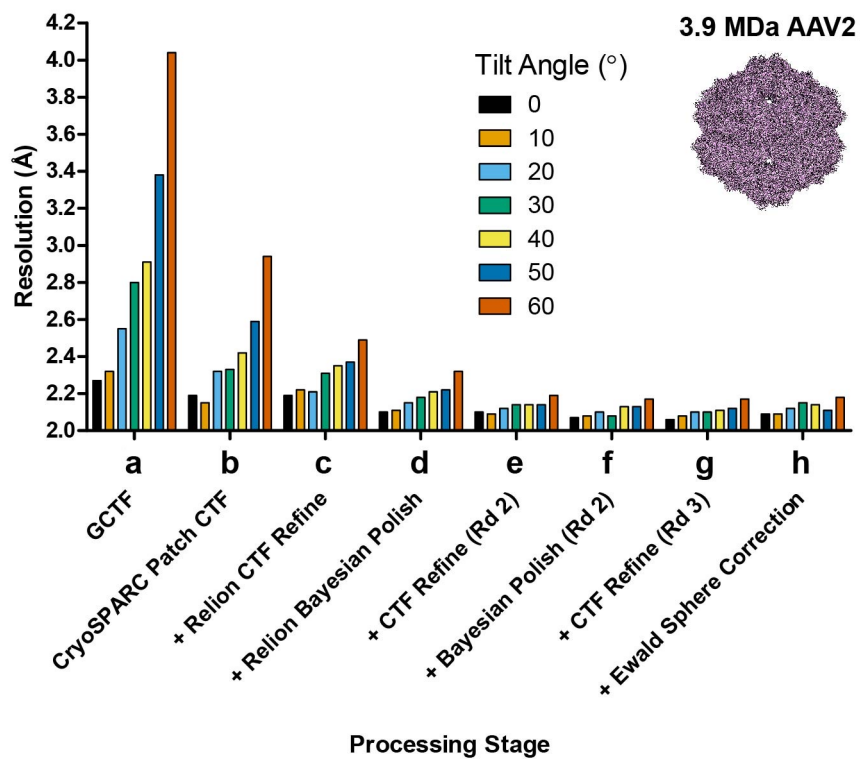
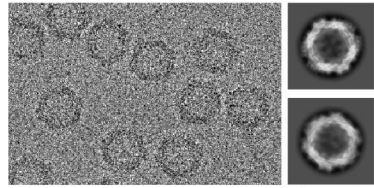


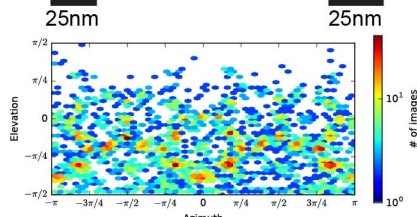
Figure 2

0° Tilt

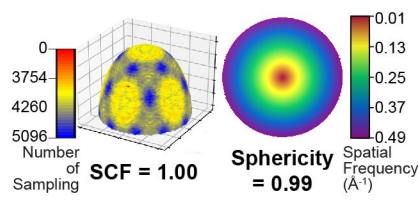
a



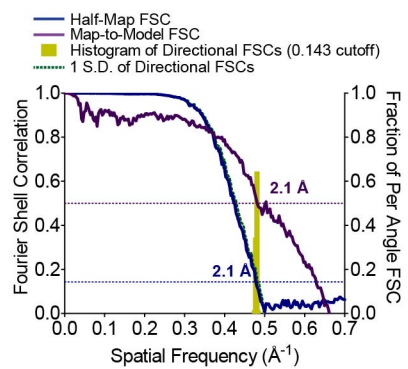
b



c

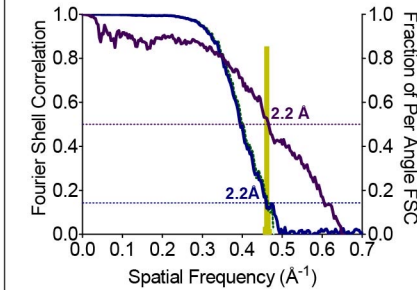
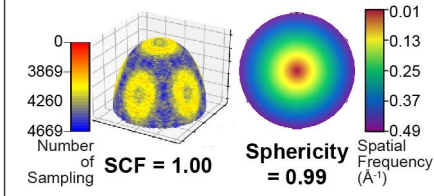
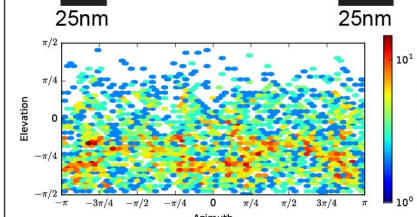
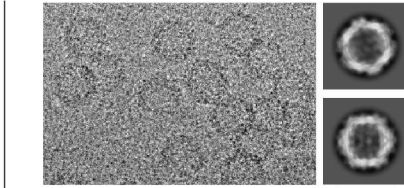
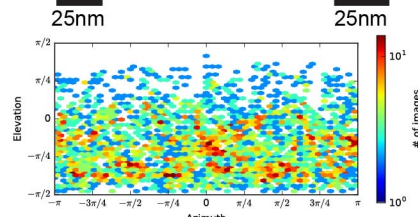
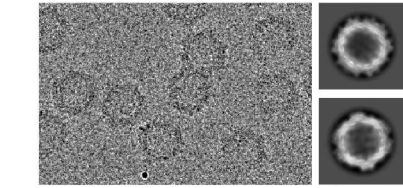


d



30° Tilt

30° Tilt



e

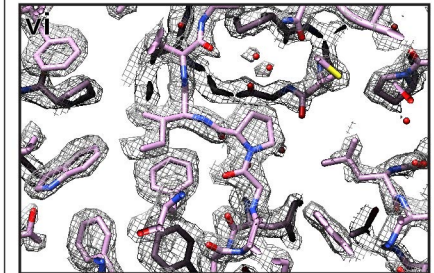
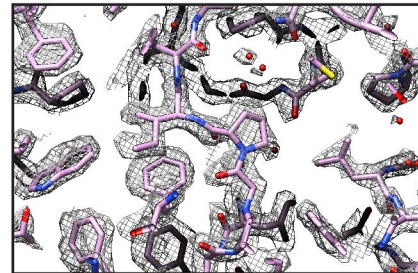
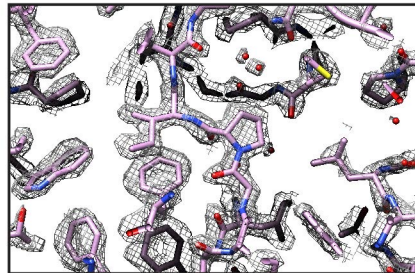


Figure 3

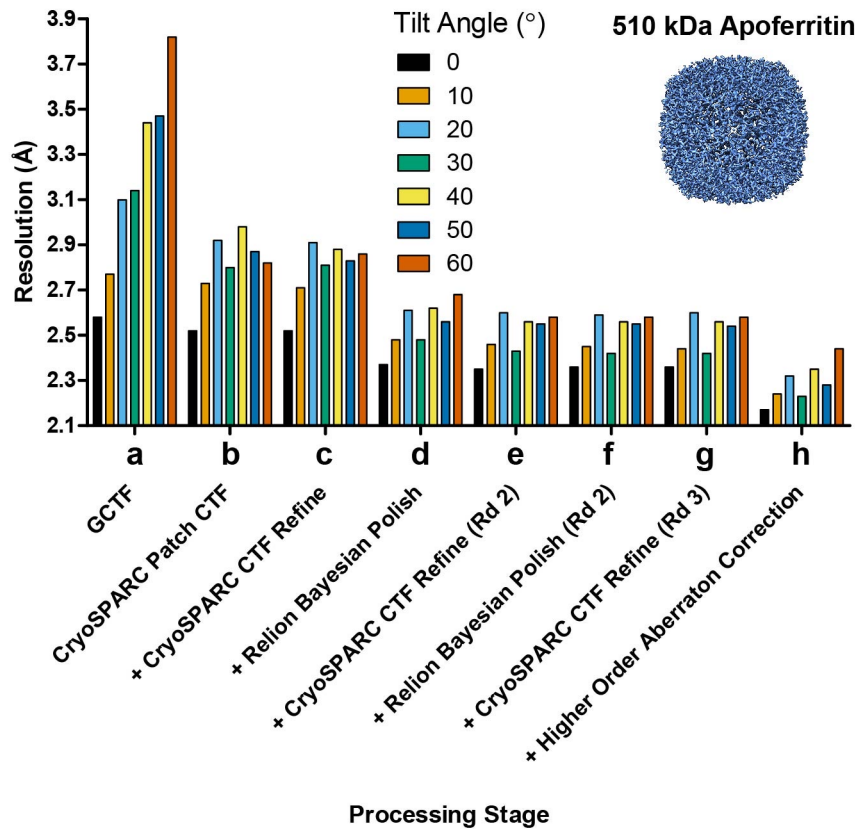
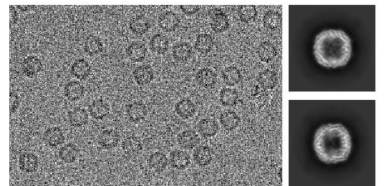


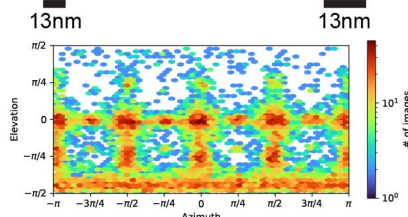
Figure 4

0° Tilt

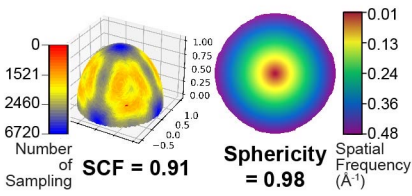
a



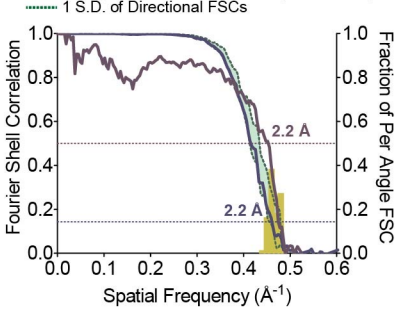
b



c

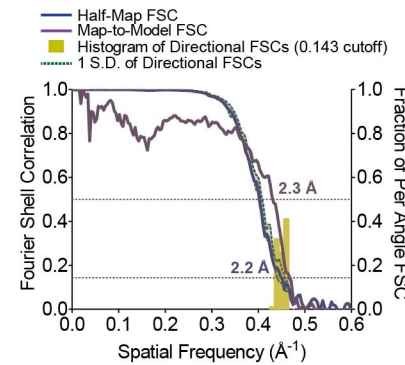
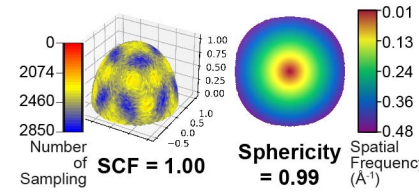
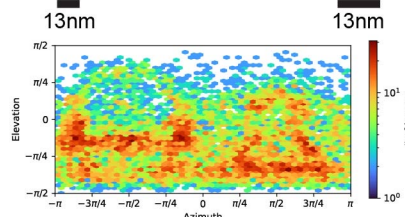
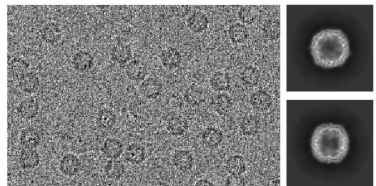


d



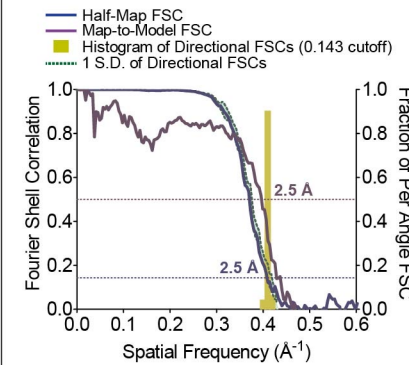
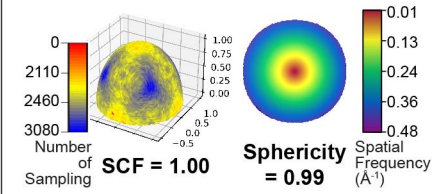
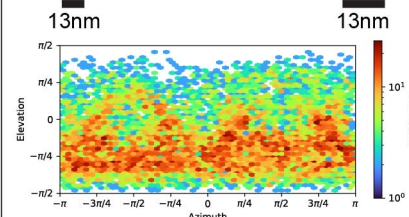
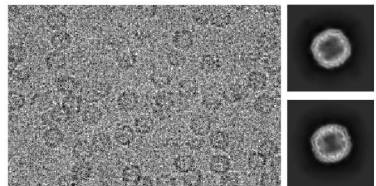
30° Tilt

a



60° Tilt

a



e

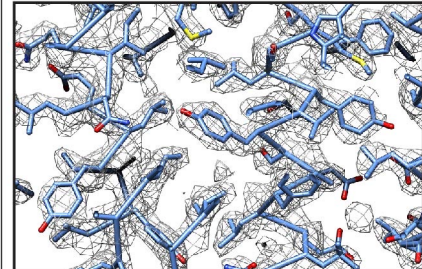
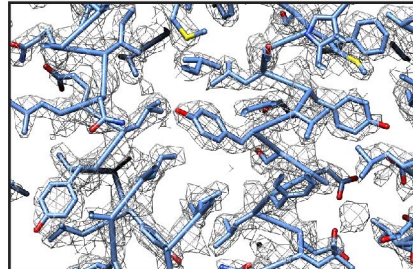
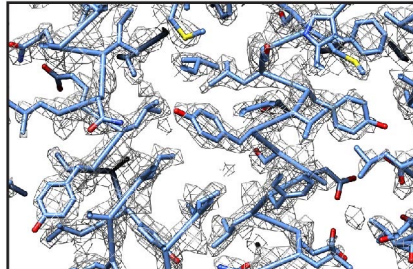


Figure 5

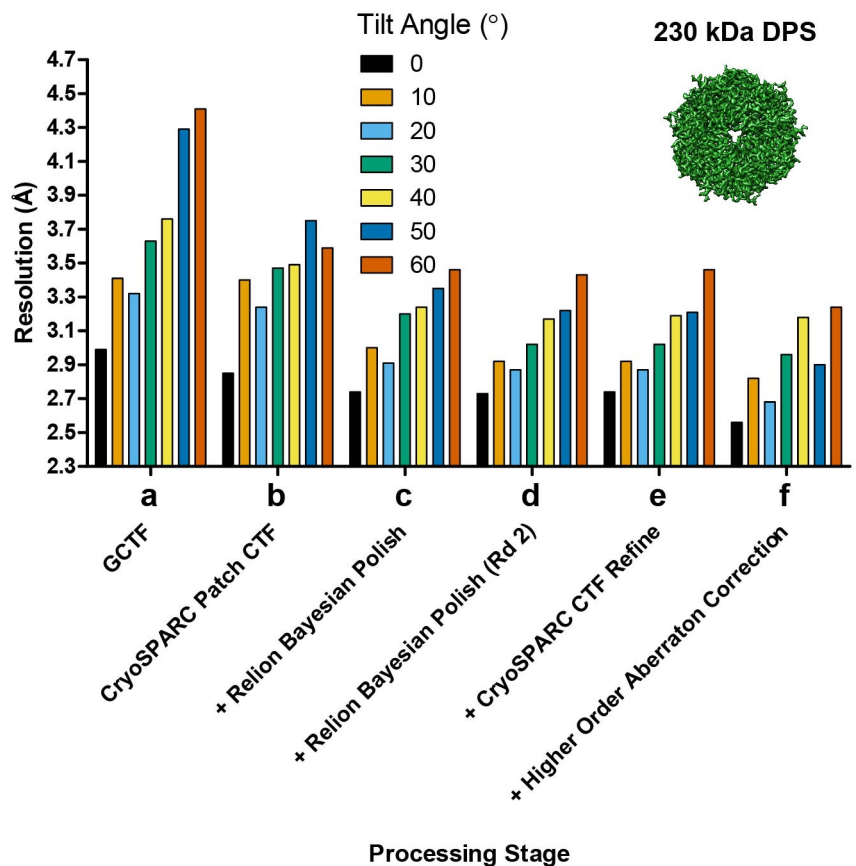


Figure 6

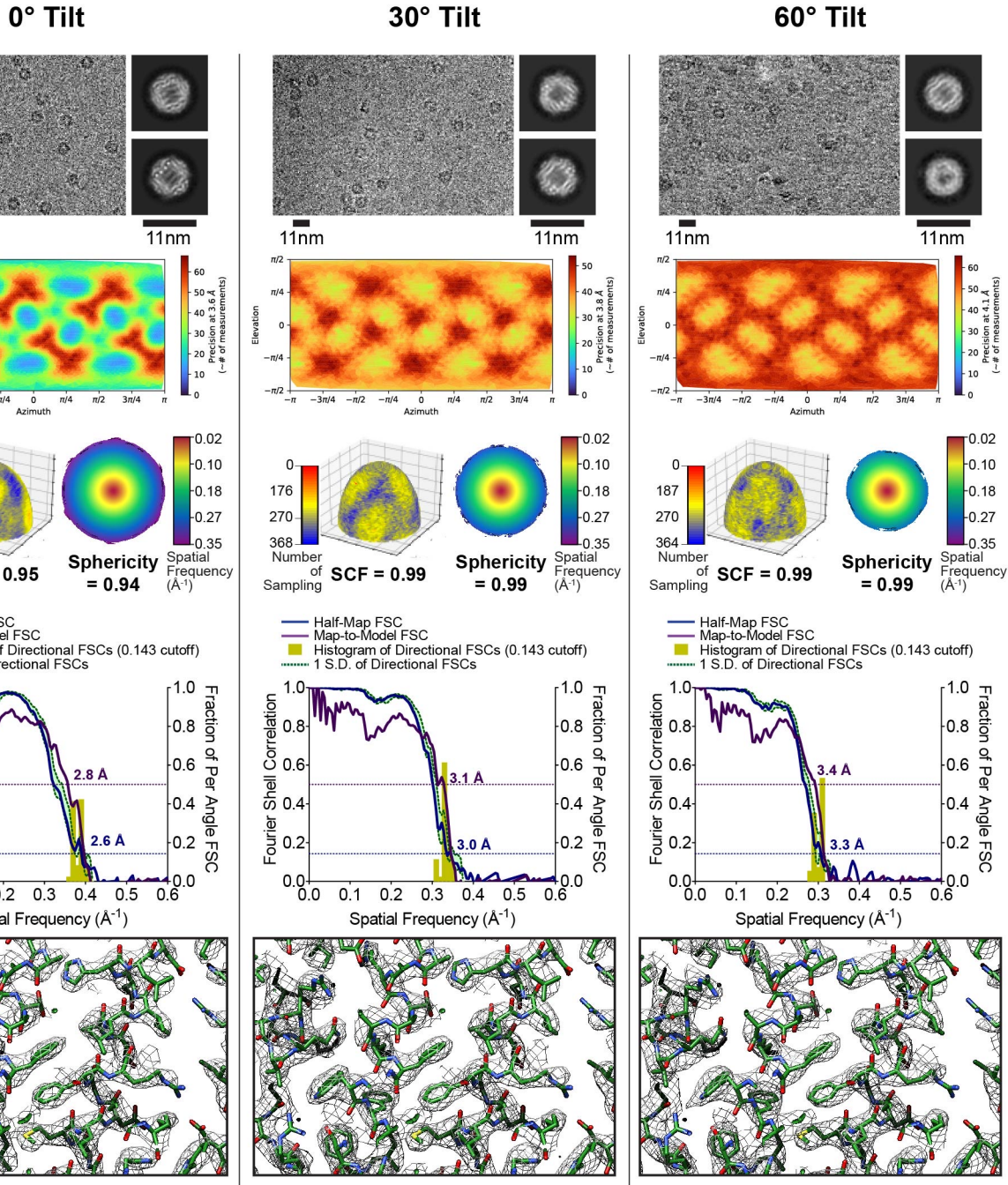


Figure 7

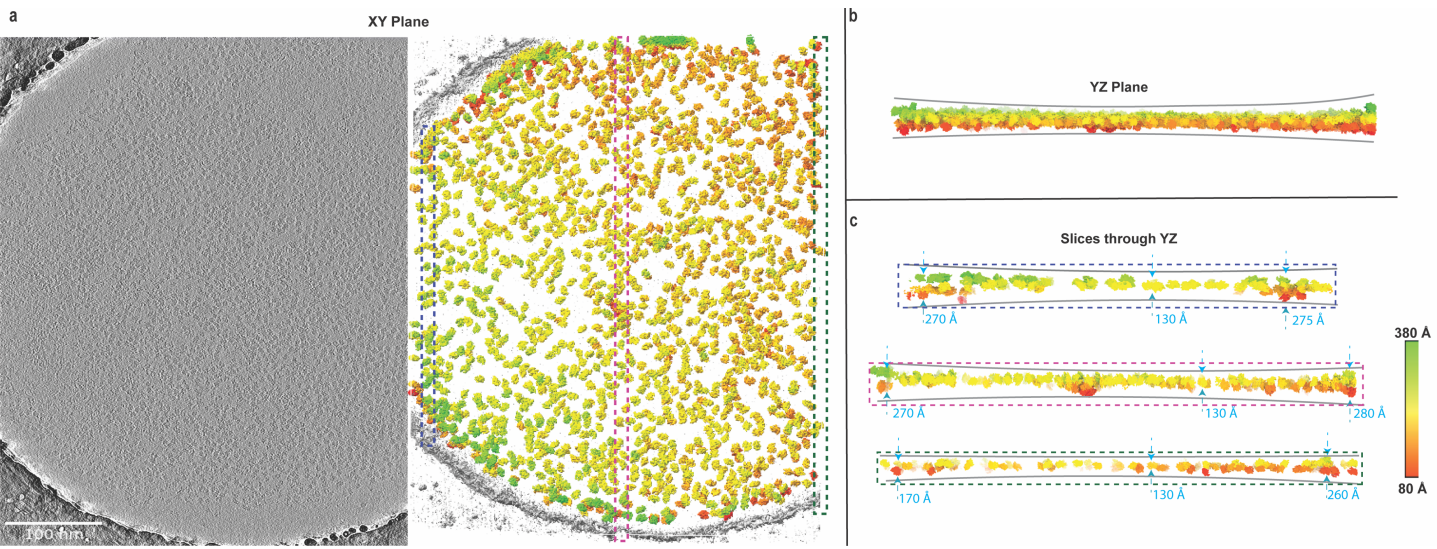


Figure 8

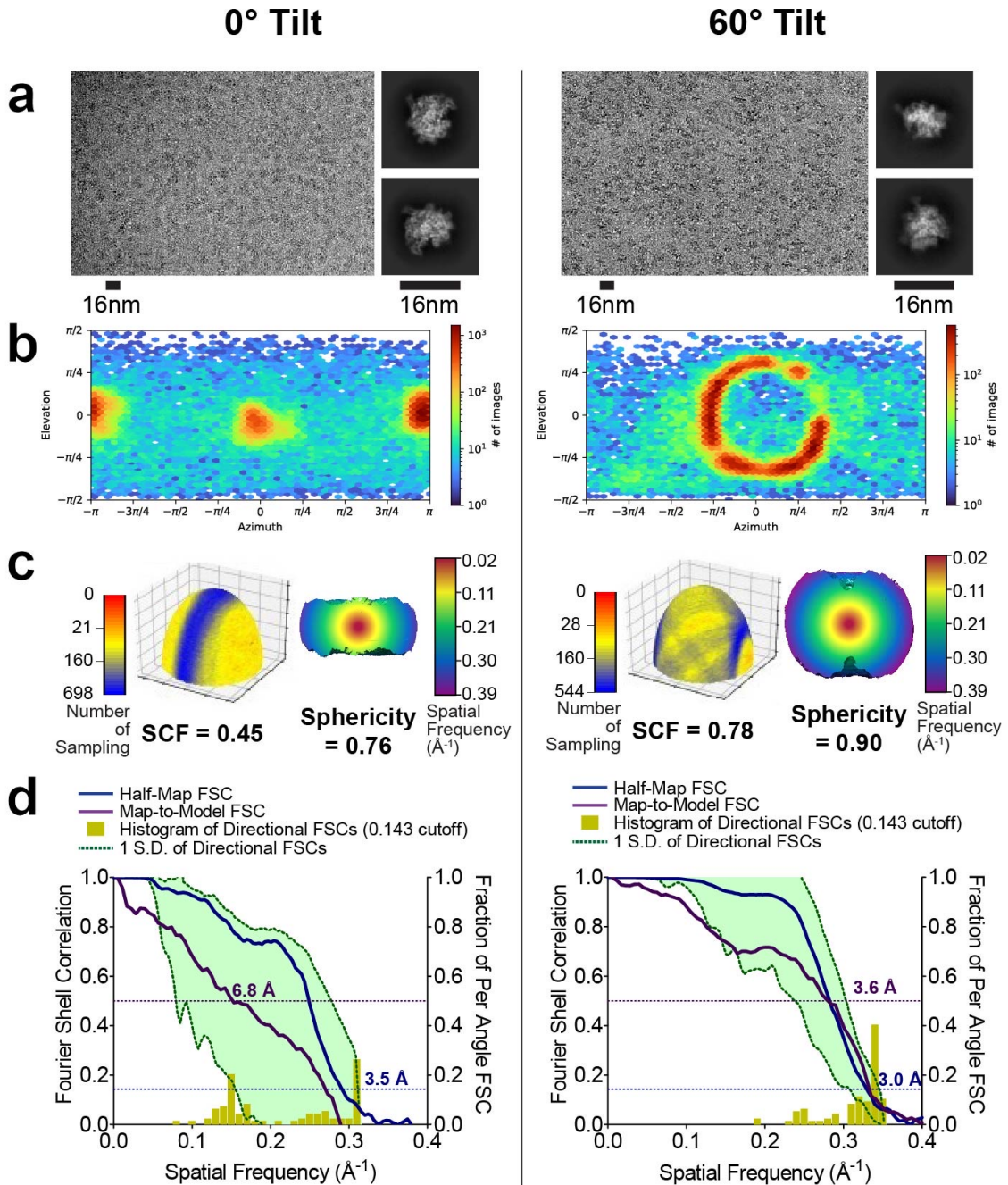


Figure 9

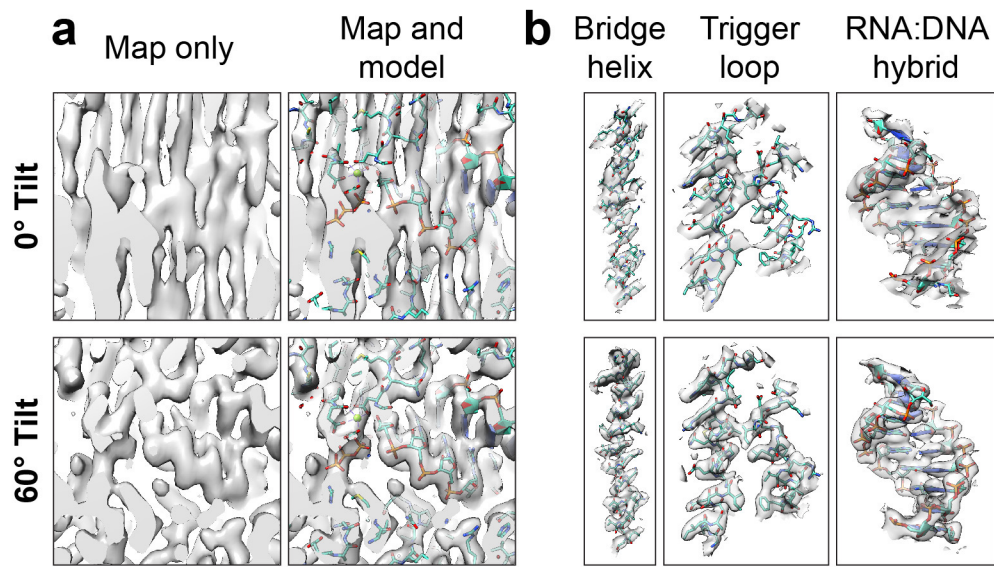


Figure 10

